Orbital-scale benthic foraminiferal oxygen isotope stratigraphy at the northern Bering Sea Slope Site U1343 (IODP Expedition 323) and its Pleistocene paleoceanographic significance

H. Asahi[1*], S. Kender[2,3], M. Ikehara[4], T. Sakamoto[5, 6], K. Takahashi[7], A.C. Ravelo[8], C.A. Alvarez Zarikian[9], B.K. Khim[10*], and M.J. Leng[2, 11]

[1] Marine Research Institute and School of Coastal Earth Environment, Pusan National University, Busan 609-735, Korea

[2] British Geological Survey, Keyworth, Nottingham NG12 5GG, UK

[3] Department of Geology, University of Leicester, Leicester LE1 7RH, UK

[4] Center for Advanced Marine Core Research, Kochi University, Nankoku 783-0093, Japan (ikheara@kochi-u.ac.jp)

[5] Mie University, Tsu City 514-8507, Japan (tats@bio.mie-u.ac.jp)

[6] Japan Agency for Marine-Earth Science and Techology (JAMSTEC), Yokosuka 237-0061, Japan

[7] Hokusei Gakuen University, Sapporo 004-8631, Japan (kozotaka@hokusei.ac.jp)

[8] University of California Santa Cruz, Santa Cruz CA 95064, USA (acr@ucsc.edu)

[9] IODP, Texas A&M University, College Station TX 77845, USA (zarikian@iodp.tamu.edu)

[10] Department of Oceanography, Pusan National University, Busan 609-735, Korea

[11] NERC Isotope Geosciences Laboratory, British Geological Survey, Nottingham NG12 5GG, UK

Corresponding authors (asahiro@pusan.ac.kr, bkkhim@pusan.ac.kr)

Abstract

A continuous composite oxygen isotope ($\delta^{18}O$) stratigraphy from benthic foraminifera in the Bering Sea was reconstructed in order to provide insight into understanding sea-ice evolution in response to Northern Hemisphere Glaciation. Oxygen isotope records from multiple species of benthic foraminifera at Integrated Ocean Drilling Program (IODP) Expedition 323 Site U1343 (54˚33.4'N, 176˚49.0' E, water depth 1950 m) yield a highly refined orbital-scale age model spanning the last 1.2 Ma, and a refined age model between 1.2 and 2.4 Ma. An inter-species calibration was used to define species offsets and to successfully obtain a continuous composite benthic $\delta^{18}O$ record, correlated with the global composite benthic $\delta^{18}O$ stack curve LR04 to construct an orbital-scale age model. The consistency of the benthic $\delta^{18}O$ stratigraphy with biostratigraphy and magnetostratigraphy confirms the reliability of both methods for constraining age. The time difference between cyclic changes in sedimentary physical properties and glacial-interglacial cycles since 0.8 Ma is notable, and suggests that physical properties alone cannot be used to construct an orbital-scale age model. Amplitude changes in physical properties and a significant drop in the linear sedimentation rate during glacials after 0.9 Ma indicate that the glacial sea-ice edge extended beyond the Bering Sea Slope (Site U1343) at this time.

Keywords: oxygen isotope stratigraphy, benthic foraminifera, Pleistocene, sea-ice, Bering Sea, IODP

1. Introduction

The construction of orbital-scale age models, particularly in the Quaternary epoch, is essential for understanding climate changes in terms of glacial and interglacial (G-IG) cycles. Comparison of benthic foraminiferal oxygen isotope ($\delta^{18}O$) data to the composite global stack curve LR04 (Lisiecki and Raymo 2005) enables establishment of a precise orbital-scale age model back to 5.3 Ma. However, it is commonly difficult to construct a continuous $\delta^{18}O$ record using a single taxon of benthic foraminifera due to changing assemblage compositions and bottom water conditions, and also due to calcite dissolution especially in regions with low calcite preservation such as the North Pacific and the Southern Ocean.

One solution is to establish composite $\delta^{18}O$ records using multiple species and inter-species calibrations. Previous comparisons between the $\delta^{18}O$ of benthic foraminiferal calcite and the $\delta^{18}O$ of bottom water in different basins demonstrated that the species-specific offsets are related to both their microhabitat and vital effects (e.g. McCorkle et al., 1990, 1997). Investigations in different basins have provided accurate species-specific offsets in the past (e.g. the Aleutian Margin and the Southern Australian Margin; Basak et al., 2009). These studies suggest the possibility that, in each specific basin, constant species offsets in $\delta^{18}O$ exist, allowing the use of $\delta^{18}O$ from different species to be compiled in order to establish continuous $\delta^{18}O$ records.

A quicker but less robust approach may be to utilize the physical properties (PP) of the sediments (e.g. Haug et al., 1995; Mix et al., 1995b; Shackleton et al., 1995). This may be tempting as it is based on an assumption of coeval changes in the sediment characteristics between G-IG cycles. For example, there is general agreement that biological production in the Bering Sea increased during interglacial periods (e.g.

Okazaki et al., 2005; Kim et al., 2011), whilst high contributions of terrigenous and glaciomarine components have been proposed during glacial periods. Changing proportions of these different sedimentary components leave signatures in the natural gamma-ray radiation (NGR), the magnetic susceptibility (MS), and the gamma ray attenuation (GRA), as these sediment properties indicate relative changes in clay minerals, glaciomarine components (e.g. ice-rafted debris: IRD), and sediment bulk composition, respectively. Furthermore, the observed cyclic alternation of the biogenic and siliciclastic sedimentary components at all seven sites drilled during IODP Expedition 323 appears to provide the potential to identify G-IG cycles (Takahashi et al., 2011; Aiello and Ravelo, 2012). However, their correlation with benthic $\delta^{18}O$ cycles is so far confirmed only back to the last interglacial (e.g. Okazaki et al., 2005; Kim et al., 2011). Therefore, further tests are required to examine whether this approach is appropriate for the ~2.4 Myr-long sedimentary record at the Bering Sea Slope Site U1343.

Previous paleoceanographic studies in the Bering Sea demonstrate that sea-ice evolution likely played an important role in regulating climate changes in the Bering Sea and subarctic North Pacific (e.g. Cook et al., 2005; Okazaki et al., 2005; Tanaka and Takahashi, 2005; Takahashi et al., 2005). The previous studies broadly indicate that an extensive sea-ice cover existed in the Bering Sea during the last glacial maximum (LGM). A recent study, combining global climate model simulations and compiled North Pacific sedimentary records, suggested that intermediate meridional overturning circulation originated in the North Pacific during Heinrich Stadial 1 (Okazaki et al., 2010), also emphasizing the importance of sea-ice evolution in the Northern Hemisphere.

Here we present the first continuous 2.4 Myr composite $\delta^{18}O$ record of benthic foraminifera from the Bering Sea (Site U1343, on a bathymertic high near the Bering

Slope). The regional species-specific $\delta^{18}O$ offsets are evaluated using multiple measurements of different species from the same sediment horizons. An orbital-scale age model at Site U1343 is then constructed by correlating our composite $\delta^{18}O$ record with the global benthic LR04 stack (Lisiecki and Raymo, 2005). With our orbital-scale age model based on $\delta^{18}O$ stratigraphy we then discuss (1) the validity of using PP data to define G-IG cycles in the high-latitude North Pacific during the last 2.4 Myrs, and (2) regional sea-ice evolution at the Bering Sea Slope (Site U1343).

2. Materials and Methods

2.1. Oceanographic setting at Site U1343

IODP Expedition 323 Site U1343 (54˚33.4'N, 176˚49.0' E, water depth 1950 m; Fig. 1) is situated on a bathymetric high near the Bering Sea Slope. Its proximal location to the modern seasonal sea-ice edge (Cavalieri et al., 1996) suggests that this site is an ideal location to monitor past sea-ice evolution. The clear separation between the Site U1343 topographic high and the Bering Sea Shelf minimizes the influence of reworked sediments from nearby shelf areas (Takahashi et al., 2011).

Surface water circulation in the Bering Sea is dominated by an anti-clockwise gyre (the Bering Sea Gyre) along the Bering Sea Slope, contributing to the main flow of the Bering Slope Current (BSC, Stabeno et al., 1999). Water exchange between the Bering Sea and the North Pacific takes place along the several paths between the Aleutian Islands (generally between 1 and 4 km water depth; Fig. 1). North Pacific surface water flows into the Bering Sea, originating from the Alaskan Stream, which runs along the southern side of the Aleutian Islands. Most of the North Pacific water, which extends to form the BSC, flows into the Bering Sea through the Amtchitka Pass, the Buldir Pass and

the Near Strait, whilst North Pacific water flows out through the Kamchatka Strait (Kinney and Maslowski, 2012).

Atmospheric forcing is one of the factors that controls the annual variation of sea-ice distribution in the modern Bering Sea (Niebauer, 1998; Zhang et al., 2010). According to long-term observations of sea-ice and the climate regime index, sea-ice cover was reduced by 5% in the eastern Bering Sea during the late 1970s, which is attributed to changes in the position of the Aleutian Low as a result of a regime shift (Niebauer, 1998). An ice-ocean coupled model confirms that sea-ice distribution in the Bering Sea is mainly governed by changes in wind-driven ice mass advection, resulting from climate variability modes such as the Pacific Decadal Oscillation (Zhang et al., 2010).

2.2. Lithostratigraphy at Site U1343

Sediments recovered at Site U1343 are classified mainly into two groups: (a) diatom-enriched mud and (b) pelagic mud (Aiello and Ravelo, 2012). Site U1343 lithology alternates between these two primary types of sediments, with only minor amounts of volcanic shards and authigenic carbonate. Smaller mean grain size and higher NGR at Site U1343, compared to the Bowers Ridge Sites U1340, U1341, and U1342 (Fig. 1), suggest a greater contribution of terrigenous clay within sediments at the Bering Sea Slope (Aiello and Ravelo, 2012). Grain size analysis on the sediments recovered during IODP Exp. 323 suggested that the clay-sized particles at the Bering Sea Slope were delivered mainly from melting sea-ice (Aiello and Ravelo, 2012). Aiello and Ravelo (2012) further argued that silt- and sand-sized siliciclastic grains, which are also the main sediment component at Site U1343, could have been delivered from resedimentation

processes via iceberg rafting. Sedimentation rates at the Bering Sea Slope (Sites U1343, U1344, and U1345) are high compared to those at the Bowers Ridge (Sites U1340, U1341, and U1342), which was attributed to greater contribution of these silisiclastic components to the Bering Sea Slope (Takahashi et al., 2011). A total of nine laminated intervals were identified at several transitions of pelagic to diatom-enriched muds above 373.2 m core composite below sea floor, method A (CCSF-A) at Site U1343 (Takahashi et al., 2011). The composite depth scale (or splice) at Site U1343 was constructed from the correlation of physical properties from three holes drilled at the site (Holes U1343A, U1343C and U1343E, Takahashi et al., 2010). The splice consists of one complete and continuous interval from the mudline (0 m) to 235 m below seafloor (mbsf) (= 269.92 m CCSF-A). Below the spliced section, cores from Hole U1343E (with unknown gaps) are appended from ~270 to 779 m CCSF-A. With a total of 745 m recovery, the drilled sediment at Site U1343 was targeted to recover a record at least back to 2.1 Ma (Teraishi et al., in press).

2.3. Oxygen isotope measurement of benthic foraminifera

In order to obtain a continuous oxygen isotope record at Site U1343, we measured oxygen isotopes using seven species of deep sea benthic foraminifera (*Cibicidoides* spp., *Elphidium batialis*, *Globobulimina pacifica, Nonionella labradorica, Planulina wuellerstorfi*, *Uvigerina bifurcata,* and *Uvigerina senticosa*). Among these species, the genus *Elphidium* is most commonly known from shallower water habitats, but *E. batialis* is a shallow infaunal, deep water species known from the deep North Pacific (Ishiwada, 1964; Keller, 1980; Matoba, 1976; Saidova, 1961). Moreover, it has been found living at depths greater than 1000 m on the Kamchatka slope of the Okhotsk

Sea (Bubenshchikova et al., 2008), another major marginal sea in the North Pacific, and it is also abundant in the mudline (coretop) samples collected at Sites U1343 and U1344 (Takahashi et al., 2011). The common occurrence of this species, and the absence of other typical shelf benthic foraminifera, indicate that *E. batialis* was not transported from the Bering shelf and upper slope. The average sampling resolution is at intervals of 0.30 m from 0 to 170 m CCSF-A, 1.4 m from 170 to 423 m CCSF-A, and 5.1 m from 423 to 770 m CCSF-A. A total of 333 samples were used to perform isotope analyses on multiple species for the evaluation of species-specific offsets.

Two to five specimens of each benthic foraminiferal species from the >250 μm size-fraction were picked under the dissecting microscope. Brown-colored foraminiferal shells were not used for oxygen isotope analyses, because these colored tests are often contaminated by authigenic carbonate formation (Cook et al., 2011; Ohkushi et al., 2005; Hoshiba et al., 2006). Cleaning and preparation treatment of benthic foraminifera followed a conventional procedure: crushing and cleaning by ultrasonification with pure H_2O and methanol (e.g. Sagawa and Ikehara, 2008). This cleaning procedure was repeated three times with pure H_2O and two times with methanol. Cleaned samples were then dried in an oven at 40˚C for at least 6 hours prior to measurement.

Among the total of 1289 oxygen isotopic measurements, 1138 analyses were performed using the GV instruments IsoPrime® with the Multicarb preparation system at the Center for Advanced Marine Core Research at Kochi University (KCC). The remaining were analyzed at the NERC Isotope Geosciences Laboratory stable isotope facility (NIGL), also using a GV instruments IsoPrime® with the Multicarb preparation system. All of the measurement results were calibrated to the VPDB standard using international standard NBS19. The analytical precision of the oxygen isotopes derived

from replicate NBS-19 measurements is ±0.06‰ at KCC and ±0.05‰ at NIGL.

2.4. Age model construction

The age model for Site U1343 was established by correlating our continuous composite $\delta^{18}O$ record to the LR04 stack (Lisiecki and Raymo 2005). The comparison was made using a dynamic program "MATCH 2.3" (Lisiecki and Lisiecki, 2002). This dynamic algorithm allows a realistic matching of paleoclimate data sets with less effort and uncertainty than the hand-tuning procedure. All data that showed any sign of contamination with anomalously low $\delta^{13}C$ (as seen in Cook et al. 2011; Ohkushi et al. 2005; Hoshiba et al. 2006) were excluded from further comparison and from the inter-species calibration. Prior to matching, all data were normalized in order to obtain a maximum matching efficiency. No age-depth tie points from datum events were provided prior to the matching process, in order to minimize potential bias.

The oxygen isotope stratigraphy in this study assumes that the timing of the G-IG cycles is globally uniform. Recent work on the comparison of benthic $\delta^{18}O$ records suggests a possible time lag of the Pacific benthic $\delta^{18}O$ records behind of those in the Atlantic back to at least 800 ka, ranging up to ~4 kyr (Lisecki and Raymo, 2009; Skinner and Shackleton, 2005). This lag occurred during deglacials, but may have varied at different deglacial terminations (Lisecki and Raymo, 2009). These time lags are still under debate and require further work particularly for early Pleistocene to late Pliocene records (see Venti et al., 2013), but due to the comparatively short duration of the potential lag we simply applied automatic matching of our $\delta^{18}O$ records to the LR04, without any manual alignment to reflect possible lags between Pacific and Atlantic.

2.5. Spectrum analysis on benthic foraminiferal $\delta^{18}O$ and physical properties

In order to quantify periodicity and time differences between $\delta^{18}O$ and PP data at Site U1343, we have employed cross spectrum analysis by using cross wavelet analysis (Torrence and Compo, 1998) and the Blackman-Tukey (B-T) cross spectrum analysis (Analyseries 2.4: Paillard et al., 1996). The cross wavelet analysis visualizes the continuous changes in the power and coherency within a time-frequency space, while the B-T cross spectrum analysis represents these changes in a designated time window. Prior to each spectrum analysis, all analyzed data were resampled at every 2 kyr by linear interpolation, approximate to the original sample interval, between 0 and 1.2 Ma. The B-T cross spectrum analysis was performed using 150 lags for a total of four different time windows (0-0.8 Ma, 0.8-1.2 Ma, 1.2-2.4 Ma, and the entire time range). Cross wavelet analysis was performed using a program code provided by C. Torrence and G. Compo (http://paos.colorad.edu/research/wavelets/software.html), using Morlet as a mother wavelet signal.

3. Results and Discussion

3.1. Inter-species calibration of benthic foraminiferal $\delta^{18}O$

Results of $\delta^{18}O$ measurements using multiple species of benthic foraminifera were compared in order to establish an orbital-scale continuous composite record (Fig. 2 and Table 1). Species-specific offsets were calculated relative to the isotopic value of *E. batialis,* which is the most abundant species present at Site U1343. The species-specific offsets between other species and *E. batialis* range from -0.15 to +0.86 ‰ (Table 1). Despite relatively large standard deviations (Table 1), there appears to be no systematic species-specific offset trend (Fig. 3a). Since most offset-corrected $\delta^{18}O$ values fall onto

the composite $\delta^{18}O$ line (Fig. 3b), this approach does not affect the overall quality of the oxygen isotope curve.

To make our results comparable with other published calibration data sets, we have calculated the $\Delta\delta^{18}O_{water\text{-}calcite}$, defined as the differences between the theoretical $\delta^{18}O$ of calcite precipitated in equilibrium and the measured $\delta^{18}O$. Since no oxygen isotope measurements of seawater are available at Site U1343, we have estimated $\Delta\delta^{18}O_{water\text{-}calcite}$ of each benthic foraminifera based upon the modern $\Delta\delta^{18}O_{water\text{-}calcite}$ of *G. pacifica* observed in the Aleutian Basin (0.21‰, Basak et al., 2009), and our species-specific offsets (Table 1).

Species-specific offsets at Site U1343 (Table 1) are comparable to previously published data (McCorkle et al., 1990; 1997), with several notable disagreements. A value of –0.64‰ is widely recognized for the offset correction between *U. peregrina* and *P. wuellerstorfi* (Shackleton, 1974; and confirmed by multiple studies such as Mix et al., 1995a, 1995b). Since *U. bifurcata* is a superficially similar morphotype to *U. peregina* (e.g. Schönfeld, 2006), and possibly combined in some studies with *U. peregina* $\delta^{18}O$ (criticized in Fontanier et al., 2008 – see below), the offset value of *U. bifurcata* to *P. wuellerstorfi* may be expected to show a similar value to that of *U. peregrina* relative to *P. wuellerstorfi*. However, at Site U1343, the offset between *U. bifurcata* and *Cibicidoides* spp. is –0.34±0.32‰ (n=36), and for *P. wuellerstorfi* it is –0.98±0.03‰ (n=2). Such a disagreement in $\delta^{18}O$ offsets between *Uvigerina* and *P. wuellerstorfi* at Site U1343 to other published offsets could be explained by (a) the uncertainties in the estimate of the species-specific offset, and/or (b) size-dependent vital effects.

There are general agreements that species-specific offsets are attributed to

differences in vital effects and that these offsets from theoretical equilibrium are fairly constant at different locations but there can be uncertainties (e.g. Fontanier et al., 2006). Large standard deviations in the $\Delta\delta^{18}O_{water\text{-}calcite}$ of *Cibicidoides* (±0.38‰, n=11) and of *U. peregrina* (±0.14‰, n=16) indicate that their uncertainties are not negligible (McCorkle et al., 1997). Furthermore, Hoogakker et al. (2010) compiled $\delta^{18}O$ values from multiple species from piston cores in the Atlantic Ocean and Indian Ocean, and showed that there is large uncertainty in the $\delta^{18}O$ offset between *C. wuellerstorfi* and *U. peregrina* (average offset 0.72‰ with standard deviation 0.35‰). Fontanier et al. (2008) attempted to explain the wide variety of previously published values of *U. peregrina* $\Delta\delta^{18}O_{water\text{-}calcite}$ from 0.02 to 0.4‰, as potentially due to the combination of several distinct species within the *U. peregrina* group. By accounting for these uncertainties, the slight overlap between the previously published *Uvigerina* offsets and the calculated *Uvigerina* offset at Site U1343 in this study could be attributed to the choice of *U. bifurcata* over *U. peregrina*.

The second possible cause for the different $\delta^{18}O$ offset between *P. wuellerstorfi* and *U. bifurcata*, compared to the well recognized offset of *P. wellerstorfi* and *U. peregrina*, relies on the size-dependent vital effect of benthic foraminifera (Schmiedl et al., 2004). Planktic foraminifera exhibit $\delta^{18}O$ values that increase with shell size due to the changing conditions that affect growth rate (Berger et al., 1978; Friedrich, et al., 2012; Spero and Lea, 1996; Vergnaud Grazzini, 1976). For benthic foraminifera, Schmiedl et al. (2004) also found a logarithmic increase in the $\delta^{18}O$ of *U. mediterranea* with increased size (1.63‰ at 175-225 µm size-fraction and 2.12‰ at 950-1050 µm size-fraction, respectively). We did not perform size-variation $\delta^{18}O$ analysis due to the relatively low abundances of small specimens in our samples. Although we cannot therefore test

whether the shell size may have an effect on $\delta^{18}O$, our analyses were all made on large (>250 μm) specimens effectively minimizing the error associated with shell size.

The general agreement between species-specific offsets for the majority of benthic foraminifera at Site U1343 and the previously published data suggests that vital effects can be considered globally uniform. Therefore, the offset values can be used to adjust the $\delta^{18}O$ values of multiple species of benthic foraminifera to be consistent with a single species $\delta^{18}O$ value, in order to establish a composite oxygen isotope record (as is commonly applied to *Uvigerina* and *Cibicidoides*, e.g. Mix et al., 1995a, b). Our results emphasize that multiple-species calibrations and precise species-specific corrections are needed to reconstruct a high quality benthic foraminiferal $\delta^{18}O$ composite record.

3.2. Orbital-scale oxygen isotope stratigraphy at Site U1343

The correlation of our Site U1343 composite benthic $\delta^{18}O$ record with the LR04 global stack curve (Lisiecki and Raymo, 2005) provides a precise orbital-scale age model (Fig. 4 and Appendix 1 and 2) that complements and confirms other stratigraphic data (i.e. diatoms, silicoflagellates and ebridians: Terashi et al., in press; calcareous nannofossils, radiolarians and paleomagnetism: Takahashi et al., 2011). Nineteen out of a total of twenty two datum events are confirmed by the orbital-scale benthic $\delta^{18}O$ age model at Site U1343, within their estimation errors. The remaining three datum events, LCO *Actinocyclus oculatus* (0.9 Ma at 314.3-322.23 m CCSF-A; Teraishi et al., in press.), LO *Filisphaera filifera* (1.4-1.7 Ma at 307.7 m CCSF-A; Takahashi et al., 2011), and FO *Eucyrtidium matuyamai* (1.7-1.9 Ma at 648.1 m CCSF-A; Takahashi et al., 2011), do not match with our benthic $\delta^{18}O$ age model (Fig. 4). These exceptional datum events, in

contrast to the majority of other datum events, appear to be less reliable in the Bering Sea than elsewhere. However, the majority of datum events are consistent with our benthic $\delta^{18}O$ age model, confirming the overall quality of both data sets. Since we did not include any datum event in the initial age-depth tie points prior to the matching, the consistent agreement between the benthic $\delta^{18}O$ stratigraphy and the other datum events suggests that our age model is reliable even in the interval of relatively low sampling (~1.2–2.4 Ma) although the resolution of our record during this interval prohibits precise orbital-scale age control.

Our newly established orbital-scale age model is based on an oxygen isotope record at Site U1343 resolved to 1.7 kyrs between 0 and 1.2 Ma (0-341 m CCSF-A), and 10.3 kyrs between 1.2 and 2.4 Ma (341-769 m CCSF-A) (Fig. 5). Each marine isotope stage (MIS) is identified in the $\delta^{18}O$ record at Site U1343 from 0-1.2 Ma, whilst prior to 1.2 Ma the record misses detection of some MISs. Despite these missing stages, no hiatus intervals were identified based on an absence of any notable jumps in calculated linear sedimentation rate (LSR) before 1.2 Ma. The missing stages at Site U1343 are therefore more likely attributed to our low-resolution records below 341 m CCSF-A.

The validity of our oxygen isotope stratigraphy is further tested by various cross-spectral analyses with LR04, and comparison of orbital-scale band pass filtered variability. Two major orbital-scale periodicities (41- and 100-kyr) for the $\delta^{18}O$ records at U1343 were recognized within different time windows (Figs. 6 and 7). The statistical significance test in continuous wavelet transform (CWT) suggests that the 100-kyr periodicity in our record was dominant since 0.7 Ma, while 41-kyr variability characterizes it since at least 1.5 Ma to the 90% confidence level (Fig. 7b). The lack of a significant presence of the 41-kyr band prior to 1.5 Ma is likely due to low sampling

resolution. Due to similar spectral variability, the coherency of our record and LR04 at the 41- and 100-kyr frequencies is high (~0.8), and nearly in-phase after 1.5 Ma (Fig. 7c), strengthening the validity of our orbital-scale oxygen isotope stratigraphy. The nearly in-phase relationship between the $\delta^{18}O$ records at U1343 and LR04 can be also seen in their band-pass filtered variability (Fig. 8), demonstrating the overall quality of our oxygen isotope stratigraphy.

Average time differences of the Site U1343 $\delta^{18}O$ record over LR04 at two major orbital-scale periodicities throughout the study periods ranged from 2.3±2.4 kyr lags at the 100-kyr band, to 2.1±1.0 kyr leads at the 41-kyr band. These numbers are fairly close to or smaller than the sampling resolution (1.9 kyr after 1.5 Ma and 10.6 kyr before 1.5 Ma), and possible time lags between the Pacific and the Atlantic records (Lisecki and Raymo, 2009), suggesting that these lead-lag differences could be within the uncertainty of our oxygen isotope stratigraphy.

3.3. Validity of PP data as the orbital scale tunings

The PP data at Site U1343 have previously been regarded as likely reflecting a change in sediment properties between G-IG cycles (e.g. Takahashi et al., 2011). At Site U1343, the natural gamma radiation (NGR) largely reflects the grain size variability within a size fraction between 0.04 μm and 2.0 mm (Aiello and Ravelo, 2012). A general coincidence in the timing between the positive peaks in % biogenic opal (Kim et al., in press) and negative peaks of gamma ray attenuation (GRA) indicate that GRA partially reflects sediment characteristics from biogenics (negative peaks) to silisiclastics (positive peaks). But a disagreement in the long-term variability of % biogenic opal and GRA indicates potential biases by other factors. The magnetic susceptibility (MS) has been

interpreted as generally reflecting glaciomarine input to the North Pacific (Haug et al., 1995), but a later study at the same site reinterpreted MS as aeolian dust input and volcaniclastic components (Bailey et al., 2011). This later reinterpreation suggested aeolian dust was a major contributer to MS vairability throughout the North Pacific region. Frequent presences of pebble-sized IRD at the Bering Sea Slope (Takahashi et al., 2011) suggests that MS at Site U1343 may more likely represent glaciomarine inputs rather than other factors.

The assumed potential coupling between the PP data and G-IG cycles can be tested with various cross spectrum analyses between PP data and $\delta^{18}O$ at Site U1343, by examining their power spectra, coherency, and lead-lag relationships. Since G-IG cycles shifted from 41 kyrs to ~100 kyrs periodicity during 0.8–1.2 Ma (so called Mid-Pleistocene Transition: MPT), we have conducted the B-T cross spectrum analysis in four different time intervals: (a) 0.8 Ma to Holocene ('100-kyr world'), (b) 1.2-0.8 Ma (transition period), (c) 2.4-1.2 Ma ('41-kyr world') and (d) the entire studied time range.

Results of two different spectrum analyses indicate the presence of orbital-scale periodicities (41-kyr and 100-kyr band) in all PP data sets, but their significance varies in different time windows (Figs. 6 and 9). B-T spectral analyses reveals the presence of both the 41-kyr and 100-kyr band periodicities in the PP data within a confidence level of 80% (Fig. 6); however, CWT analyses, using a red noise as the background signal, does not agree with the B-T spectral analyses results (Fig. 9).

These differerent results are attributed to different approach on its significant test on each spectrum analysis, which further can be related to the choise of the background signal. In this study, there are two background noise concerned: (a) white-noise signal containing random noise at any frequency domain; and (b) red-noise signal containing

general decreasing trend along the freqeuncy increase. The significant test on the B-T spectrum uses estimation uncertanities of spectrum power to visualize how each spectrum peak signifies from its power nearby subject frequency. Therefore, our approach in the B-T spectrum is similar to the test with the white-noise signal. At Site U1343, B-T spectrum powers of GRA and NGR during 0-0.8 Ma and 0.8-1.2 Ma intervals showed a less decreasing trend than those of MS and $\delta^{18}O$ (Fig. 6). This trend is rather similar to the tendency of the white-noise signal than that of the red-noise signal. In such a case, any periodical change at low frequency is not likely detected by the red-noise signal test, due to their low spectral powers. On the other hand, a signal with the red-noise tends to show large amplitude at low frequency (a long-lasting trend) domain, that can be integrated or modulated from periodical changes at higher frequency. Any change in period detected by this test would tend to be signigicant with respect to the original time series (as seen in the 100-kyr periodical change in $\delta^{18}O$ after 1.2 Ma). Such different signatures of these background signals need to be concerned, when evaluating the significance of each periodical change.

According to the red-noise significance test, all PP data exhibited significant periodicity at either 41-kyr and/or 100-kyr band. However, recognition in frequency-time space varies at different time intervals. GRA and NGR show significant power at the 41-kyr band only during 1.2-2.4 Ma (Fig. 9). These significant periodicities need to be evaluated with caution due to the large uncertainty in the age model. However, the fact that there are no significant long-term increases or decreases in the LSR during that interval (Fig. 5) suggests that any uncertainty in the age model is limited to one G-IG cycle (~41 kyr). This maximum estimation suggests that such an age-model uncertanity should not affect the presence of significant power at the ~41-kyr band. Furthermore,

distinct peaks in the NGR and GRA visible during the 1.2-2.4 Ma interval (Fig. 5) confirms the likely presence of such periodic changes. Potential age model uncertainty effects during the interval 1.2-2.4 Ma include their sigfinicant powers in a wide range of frequencies (Fig. 9), and their diversed phase angles (Figs. 10b and 10c). We would expect that high spectral power will converge on a particular frequency once a more refined age-model is established during this interval. Consequently, an enhanced oxygen isotope stratigraphy for the older section of U1343 is needed to provide clearer interpretations of the periodic variations during that interval.

Unlike the NGR and GRA records, variability between MS and the $\delta^{18}O$ is similar, with significant 41-kyr periodicity during 0.8-1.3 Ma and after 0.6 Ma, and significant 100-kyr periodicity after 0.6 Ma (Fig. 9). The high coherency between the MS and the $\delta^{18}O$ after 1.0 Ma shows a coupling of the MS with G-IG cycles (Fig. 10c). Their phase angles exhibit a gradual change from 90˚ lag to nearly in phase after 1.0 Ma (Fig. 10c), which is approximately 0-20 kyr lags to the $\delta^{18}O$ record. Since the age model during such periods is well constrained, this variability in phase angle implies that their lead-lag relationships can vary at different time windows. These findings suggest a potential usability of the MS to establish the orbital-scale age model. However, its application is only favorable within a limited time interval, and their variable lags to the G-IG cycle should be carefully taken into account.

The inconsistencies between PP and $\delta^{18}O$ periodicities at Site U1343 are likely attributed to differences in amplitude variability at each frequency domain. Compared to $\delta^{18}O$ and MS records, band-pass filtered NGR and GRA at both 100-kyr and 41-kyr bands represent less variability in their amplitudes during last 2.5 Myrs (Fig. 8). Since a red-noise signal test assumes that the spectrum power in a relevant time series grows with

increasing period (Rudnick and Davis, 2003), this reduction of the NGR and GRA spectrum power at the 41-kyr and 100-kyr band effects the total shape of their spectrum, thus resulting in their lack of significance when a red-noise signal test is applied. Recognition of orbital-scale periodicities (41-kyr and 100-kyr) in NGR and GRA by a white noise test indicates that there may be some potential for their use for orbital tuning. Some levels of coherency in NGR and GRA to $\delta^{18}O$ are present (Fig. 10) and more significant than the white-noise test.

At Site U1343, PP records have similar periodicities to those of the G-IG $\delta^{18}O$ records, with high coherencies exceeding 95% confidence level, by B-T cross spectrum analysis. However, PP variability is not always in phase with $\delta^{18}O$ variability (Figs 5, 10 and 11). In the 100-kyr band during the '100-ky world' (1.2 Ma to Holocene), the lag between $\delta^{18}O$ variations relative to those in NGR and GRA differs in one time interval compared to another. Specifically, in the younger portion of the record from 0.8 Ma to the Holocene, NGR and GRA variations lead those in the $\delta^{18}O$ record by 16.4±4.6 kyr and 9.6±4.3 kyr, respectively, whilst during the time interval from 1.2 to 0.8 Ma, the NGR and GRA variations lag those in the $\delta^{18}O$ record by 7.0±3.7 kyr and 8.9±5.8 kyr, respectively (Fig. 11). In contrast, MS variability lags the $\delta^{18}O$ record by 10.5±3.7 kyr during 0.8 Ma to the Holocene and by 18.2±4.1 kyr during 1.2-0.8 Ma (Fig. 11). There are several time intervals when the PP and the $\delta^{18}O$ records do not co-vary. Firstly, there are peaks in the NGR and GRA records during the transition period from glacial to interglacial, most notably at 12.4 ka but also at around 132 ka (Fig. 5). Secondly, the NGR and GRA records show gradually increasing trends in several glacial intervals (Fig. 5: MIS 2, 6, 16 for both NGR and GRA, and MIS 12 for NGR). These two trends are likely responsible for the

inconsistent lag between the PP data and the $\delta^{18}O$ record in the 100 kyr-world.

In contrast to the 100-ky band, PP and $\delta^{18}O$ variations in the 41-kyr band are nearly in phase (NGR: 1.6±1.5 kyr lags; GRA: 0.0±1.6 kyr lags) during the 41-kyr world (2.4-0.8 Ma) (Fig. 11). During the interval 1.2 to 0.8 Ma, the NGR and GRA cyclicity lags behind $\delta^{18}O$ cyclicity by only 3.1±2.8 kyr and 0.6±2.6 kyr, respectively. The various phase lags between the NGR variability and the GRA variability, compared with the $\delta^{18}O$ cycles within different time domains, indicate that there is an inconsistent phasing between changes in sedimentological characteristics and $\delta^{18}O$ cycles at the Bering Sea Slope.

There appears to be two possible explanations for the asynchrony of PP variability relative to $\delta^{18}O$ cycles within the 100-kyr world. The first relates to the biological response during the deglaciation, and the second relates to the evolution of sea-ice at the Bering Sea Slope and related sedimentation. Notably, high biological production during the last deglacial period has been reported along the northern margin of the North Pacific including the Bering Sea (Cook et al., 2005, Gebhardt et al., 2008, Gorbarenko et al., 2002, 2004, and 2005, Kim et al 2011, Okazaki et al., 2006; Ono et al., 2005; Schulung et al., 2012). This significant increase in biological production during the deglaciation is also confirmed by the coexistence of the laminated sediments at the same horizons (Cook et al., 2005; Kim et al., 2011). At Site U1343, a total of nine laminated intervals were recognized (at 10.2, 13.4, 14.1, 132, 144, 179, 424, 495 and 1266 ka, Takahashi et al., 2011). At those laminated intervals, the NGR and GRA show either (a) notable negative peaks (12.4 ka and 132 ka), or (b) gradual decreasing trends during glacial periods that contain laminated intervals (Fig. 5). The notable negative anomaly is

likely related to an abrupt increase in biological production. The presence of these notable peaks during the deglacial period produces the apparent lead of NGR and GRA variations relative to $\delta^{18}O$ variations. However, presence of the laminated intervals does not account for the gradual decreasing trend during the glacial periods, for which an alternate second mechanism is needed.

The second mechanism involves a change in sediment characteristics in association with sea-ice evolution. There appears to be a general decrease in the amplitudes of the NGR and GRA after 1.2-0.8 Ma, whilst there is a general increase in the MS amplitude (Figs. 5, 8 and 9). These amplitude changes suggest a shift in the sediment lithology, from an alternation of diatom-enriched and terrigenous-enriched sediments before ~0.9 Ma to an alternation of glaciomarine and non-glaicomarine sediments after ~0.8 Ma. This shift in the sediment characteristics is also consistent with a drop in the LSR during glacials after 0.9 Ma, suggesting that the sea-ice coverage over the Bering Sea Slope since that time has influenced the biogenic and terrigenous sedimentation at Site U1343. The gradual weakening of the NGR and GRA variations is also confirmed by the decrease in biogenic opal content at Site U1343 (Kanematsu et al., 2013; Kim et al., in press). Despite the decrease in the G-IG amplitude of the biogenic opal content, Kim et al. (in press) show that variations in biogenic opal contents are reasonably coeval with G-IG cycles throughout the last 2.4 Ma. They also find that the 100-kyr cyclicity during the 100-kyr world is not as significant as expected, consistent with the weaker 100-kyr amplitude in the NGR and GRA during ~0.8 Ma (Figs 8 and 9). Several lines of evidence, from the PP data, biogenic opal content and LSR, imply that the sea-ice cover over the Bering Sea Slope inhibited terrigenous and biogenic sedimentation, thereby weakening the NGR and GRA signals with respect to G-IG cycles. Asynchrony of the NGR and the

GRA changes relative to those in $\delta^{18}O$ at Site U1343 strongly demonstrates that direct matching of NGR and GRA to the global stack curve LR04, without any age constraints, cannot be used to establish an orbital-scale age model at the Bering Sea Slope. The presence of laminated sediment intervals and the inhibition of biogenic and terrigenous sedimentation (due to sea-ice cover) during the 100-kyr world, are two plausible influences on the NGR and GRA signals that make them asynchronous with $\delta^{18}O$ cycles.

The PP and $\delta^{18}O$ asynchrony is also reported elsewhere in the North Pacific (Bailey et al., 2011; Venti and Billup, 2012; Zahn and Mix, 1991), suggesting PP data's broadly limited utility when establishing orbital-scale age models. This is partially due to either (a) a complex relationship between PP and sediment characteristics and (b) a regional sedimentation process that may bias the PP data. For example, Haug et al. (1995) originally suggested that MS reflected glaciomarine inputs at Detroit Seamount (Site 882), but a later study revealed that MS at this site likely reflected changes in aeolian dust and volcanic ash contents (Bailey et al., 2011). At Site U1343, however, the application of this interpretation for MS is not appropriate due to the relatively minor contribution from volcaniclastics (Takahashi et al., 2011). Moreover, MS variability with G-IG cycles at U1343 is likely antiphased with observed eolian dust fluxes to the North Pacific (Hovan et al., 1991; Bailey et al., 2011) and Chinese loess sequences (Kukla and An, 1989; Sun and An, 2005). This antiphase relationship between ocean-scale aeolian dust fluxes and MS variability at U1343 likely indicates that eolian dust is a minor contributor to MS variability. Instead, this asynchrony between PP (NGR and GRA) and $\delta^{18}O$ is due to regional sedimentation processes, associated with sea-ice expansion after 0.9 Ma at the Bering Sea Slope. Large glaciomarine contributions at Site U1343 may have overridden any potential original G-IG cycle synchronicity of NGR and GRA after 0.9 Ma. Similar

findings of a decoupling between PP and G-IG cycles in the North Pacific (see above) demonstrate a limitation of PP data for orbital-scale age model construction, and highlight the limitation of using PP data in isolation for the evaluation of any other causal mechanisms.

3.4. Sea-ice evolution at the Bering Sea Slope during last 2.4 Myrs

Sedimentary PP records at Site U1343, with newly established orbital-scale oxygen isotope stratigraphy, provide essential information to understand sea-ice evolution at the Bering Sea Slope during the last 2.4 Myrs. The most notable changes in our data occurred within the interval 1.4-0.9 Ma, as evidenced by a drop in LSR (mainly during glacial periods), a decrease in amplitude of NGR and GRA variability, and increases in MS values and amplitude of variation (Figs. 5, 8, 9 and 12). A gradual increase in MS indicates a marked increase of the contribution of glaciomarine sediments, whilst changes in the amplitudes of the NGR, GRA and MS suggest that variations in glaciomarine input controlled the main sediment characteristics after 0.8 Ma. Since glaciomarine input is mainly regulated by the distance from the sea-ice edge, where most of the seasonal sea-ice melting occurs (Sakamoto et al., 2005), this notable shift in the sediment characteristics is likely due to changes in the sea-ice conditions at the Bering Sea Slope during that period. This proposed sea-ice extension is also consistent with the stepwise increase in the abundance of sea-ice diatoms during 1.2-0.9 Ma at Site U1343 (Teraishi et al., in press). During the same period of this increase, the inflow from the North Pacific via the Alaskan Stream was notably reduced, as indicated by a decrease in pelagic diatoms (Teraishi et al., in press). The relatively large NGR and GRA amplitudes prior to 1.2 Ma (Figs. 5, 8, 9 and 12) imply that the seasonal sea-ice maxima did not reach

the Bering Sea Slope, as it does today, possibly due to strong inflow of relatively warm water from the North Pacific, prior to 1.2 Ma.

In contrast, the amplitude of NGR, GRA, and MS variability changed after 0.8 Ma, indicating that sea-ice expanded over the Aleutian Basin, as North Pacific water inflow decreased, during glacials. In the MS record, there are notable spikes during interglacial periods at Site U1343 (Figs 5 and 12), most likely reflecting coarse-grained particles supplied by glaciomarine input due to *in situ* sea-ice melting over the Bering Sea Slope. Marked high coherency between the MS and $\delta^{18}O$ after 0.8 Ma suggests that the sea-ice evolution over the Bering Sea Slope may have been governed primarily by G-IG cycles (Fig. 10c). During such intervals, their lags suggest the sea-ice edge reached the Bering Sea Slope during the transition interval from interglacials to the glacials. Gradual change in their lags after 0.6 Ma implies further extension of the sea-ice over the Bering Sea Slope at the G-IG cycle scale, as the arrival timing of the sea-ice edge became closer to the interglacial maximum. This evidence of *in situ* sea-ice melting can be further interpreted as the presence of semi-perennial sea-ice cover over the Bering Sea Slope, which likely blocked North Pacific water inflow through the Aleutian Islands during glacial periods. We propose that extensive sea-ice expansion in the Bering Sea after ~1.2-0.9 Ma prevented terrigenous and biological sedimentation, as indicated by an abrupt drop in the LSR during glacial periods, a decrease in the amplitude of the NGR and GRA, and decreased biogenic opal content (Kanematsu et al., 2013; Kim et al., in press). Semi-perennial sea-ice cover over the Bering Sea Slope during glacial periods is consistent with previously published sea-ice reconstructions during the LGM at the Bering Sea Slope (Katsuki and Takahashi, 2005; Kim et al., 2011; Rella et al., 2012) and the Umnak Plateau (Cassie et al., 2010), and suggests that the extensive sea-ice cover

over the Bering Sea documented previously only for the last glacial cycle first appeared during glacials at ~0.9 Ma.

The marked sea-ice expansion over the Bering Sea between 1.2 and 0.9 Ma can be linked to two climatic forces: (a) atmospheric forcing and (b) global continental ice sheet evolution. Modern sea-ice distribution in the Bering Sea is mainly regulated by the strength of the northerly wind in the Bering Sea during winter (Pease, 1980). This winter northerly wind, linked to location and intensity of the Siberian High and the Aleutian Low (Overland et al., 1999; Rodionov et al., 2007), enhances the southward sea-ice advection in the Bering Shelf (Zhang et al., 2010). This ocean-atmosphere linkage is also important on geological timescales as indicated by data from the Holocene (Clegg et al., 2011; Katsuki et al., 2009; Muhs et al., 2003) and the last 60 kyrs (Rella et al., 2012). The expansion of sea-ice evident in our records suggests that a similar sea-ice atmosphere linkage may have been active at least since 0.9 Ma. Since such sea-ice atmosphere linkages also impact ocean heat capacity (Zhang et al., 2010), they could be studied further in the future using SST reconstructions at Site U1343.

This extensive sea-ice expansion over the Bering Sea also coincided relatively closely with expansion of the North America Ice Sheet (Bintanja and van de Wal, 2008), suggesting a coupling between North America Ice Sheet growth and sea-ice expansion. Clark et al. (2006) hypothesized that the erosion of regolith beneath continental ice sheets in the Northern Hemisphere during the MPT (1.2-0.8 Ma) allowed ice sheets to grow thicker, overriding 41-kyr insolation cycles. However, their instability was proposed to have increased due to the basal pressure-melting in the latter stages of glacials, as a plausible driving force shifting G-IG cyclicity from 41-kyr to 100-kyr periodicity during the MPT. Elderfield et al. (2012) alternatively emphasized that an abrupt increase in

Antarctic ice volume at ~0.9 Ma initiated the shift in cyclicity during the MPT. We find evidence for an alternative hypothesis that, if sea-ice expansion over the Bering Sea Slope signifies a general expansion of sea-ice in the North Pacific region during the MPT, activation of the 'sea-ice switch' may have driven the change from 41-kyr to 100-kyr G-IG cyclicity over the MPT as proposed by Tziperman and Gildor (2003). To test this hypothesis and to determine the lead/lag and precise timing of sea-ice expansion relative to G-IG cycles during the MPT, further high-resolution studies of sea-ice over the Bering Sea Slope are needed.

4. Conclusions

An oxygen isotope stratigraphy at IODP Expedition 323 Site U1343 was established on the basis of benthic foraminiferal $\delta^{18}O$ records from seven species of benthic foraminifera (*E. batialis, U. bifurcata, G. pacifica, U. senticosa, P. wuellerstorfi, N. labradorica,* and *Cibicidoides* spp.). Comparison of $\delta^{18}O$ values from these benthic foraminifera from the same sediment horizons shows offsets that are in general agreement with other previously published data. This indicates that our multiple-species $\delta^{18}O$ data can be simply corrected with species-specific offsets in order to build an accurate composite benthic $\delta^{18}O$ record.

The benthic $\delta^{18}O$ stratigraphy at Site U1343 was constructed by correlating our composite benthic $\delta^{18}O$ record with the global benthic $\delta^{18}O$ stack LR04, which broadly converges with age models provided by biostratigraphy and paleomagnetism, suggesting that these methods are generally reliable for constraining the long-term ages. According to our composite benthic $\delta^{18}O$ age model (independent from other age markers), the

sedimentary record at Site U1343 contains a continuous paleoceanographic information of the last 2.4 Myrs.

Detailed examination of physical property (PP) records with the benthic $\delta^{18}O$ stratigraphy demonstrates notable uncertainty when using PP data to construct glacial and interglacial (G-IG) cycles. In contrast to the basic assumption of coeval changes between G-IG cycles, PP data tends to lead G-IG cycles by ~10 kyr, particularly during the last 0.8 Ma. Furthermore, this leading trend varies in different time-windows. Our study strongly indicates that direct correlation of PP data to LR04 without any age constraints (e.g. from $\delta^{18}O$) is not suitable for constructing orbital-scale chronostratigraphy. A shift toward a decreasing trend in the amplitude of the GRA and NGR with respect to G-IG cycles, a gradual increasing trend in the MS, and an abrupt drop in the linear sedimentation rate during glacials indicate that the glacial sea-ice edge likely exceeded the Bering Sea Slope by ~0.9 Ma. This extensive sea-ice expansion over the Bering Sea Slope during 0.9-1.2 Ma is likely to have been at least partially driven by atmospheric forcing over the Bering Sea. Evidence for coeval growth of North America Ice Sheet with this secular glacial sea-ice expansion in the Bering Sea suggests interaction between the sea-ice evolution in the Bering Sea and the global glacial expansions during the Mid-Pleistocene Transition.

Acknowledgement

We would like to show our great appreciation to all of the scientists, technicians, and crew of D/V JOIDES resolution during IODP Expedition 323 in the Bering Sea. We would also like to thank the curatorial staff at the Kochi Core Center for their great support in sediment sampling. Great thanks also to technical supporting members at the Center for Advanced Marine Core Research (Kochi University), especially to M.

Kobayashi, K. Suenobu, Y. Fujimura, M. Sasaoka, and M. Hamada for their assistance in sample processing and isotope measurements. The constructive reviews of Dr. N.L. Venti and an anonymous reviewer helped to improve this manuscript substantially. HA, MI, TS, and KT would like to thank to the financial aid from the supporting program for the IODP shipboard scientists by J-DESC. This research was supported by the Center for Atmospheric Sciences and Earthquake Research (Grant No. CATER 2012-040 to BKK), by Pusan National University in the programme Post-Doc. 2012 (to HA), by the NERC Isotope Geosciences Laboratory (Grant No. IP-1141-1109 to SK), by the financial aid of Kochi University (the research support program to MI), and by Japanese Ministry of Education, Culture, Sports, and Technology (the Grant-in-Aid for Scientific Research (A) #23241015 to TS). SK publishes with permission of the Executive Director of the British Geological Survey (NERC).

References

Aiello, I., Ravelo, A.C. (2012). Evolution of marine sedimentation in the Bering Sea since the Pliocene, Geosphere, 8, 6, 1-23.

Bailey, I., Liu, Q., Swann, G.E.A., Jiang, Z., Sun, Y., Zhao, X., and Roberts, A.P. (2011). Iron fertilization and biogeochemical cycles in the sub-Arctic northwest Pacific during the last Pliocene intensification of northern hemisphere glacialtion, Earth and Planetary Science Letters, 307:253-265.

Basak, C., Rathburn, A.E., Pérez, M.E, Martin, J.B., Kluesner, J.W., Levin, L.A., De Deckker, P., Gieskens, J.M., Abriani, M. (2009). Carbon and oxygen isotope geochemistry of live (stained) benthic foraminifera from the Aleutian Margin and the Southern Austrarlian Margin. Marine Mircropaleontology, 70, 89-101.

Berger, W.H., Killingley, J.S., Vincent, E. (1978). Stable isotopes in deep-sea carbonates: Box core ERDC-92, west equatorial Pacific. Oceanologica Acta 1, 203-216.

Bintanja, R., van de Wal, R.S.W. (2008). North America ice-sheet dynamics and the onset of 100,000-year glacial cycles, Nature, 454, 869-872.

Bubenshchikova, N., Nürnberg, D., Lembke-Jene, L., Pavlova, G. (2008). Living benthic foraminifera of the Okhotsk Sea: Faunal composition, standing stocks and microhabitats, Marine Micropaleontology, 69, 314-333

Caissie, B.E., Brigham-Grette, J., Lawrence, K.T., Herbert, T.D., Cook, M.S. (2010). Last Glacial Maximum to Holocene sea surface conditions at Umnak Plateau, Bering Sea, as inferred from diatom, alkenone, and stable isotope records. Paleoceanography, 25, PA1206, doi:10.1029/2008PA001671.

Cavalieri, D., Parkinson, C., Gloersen, P., Zwally, H.J. (1996, updated yearly). Sea Ice Concentrations from Nimbus-7 SMMR and DMSP SSM/I-SSMIS Passive Microwave Data, [list dates of temporal coverage used]. Boulder, Colorado USA: National Snow and Ice Data Center. Digital media.

Clark, P.U., Archern D., Polalrd, D., Blum, J.D., Rial, J.A., Brovkin, V., Mix, A.C., Pisias, N.G., Roy, M. (2006). The middle Pleistocene transition: characteristics, mechanisms, and implications for long-term changes in atmospheric pCO_2. Quaternary Science Reviews, 25, 3150-3184.

Clegg, B.F., Kelly, R., Clarke,G.H., Walker, I.R., Hu, F. S. (2011). Nonliniear response of summer temperature to Holocene insolation forcing in Alaska. Proceedings of the National Academy of Science, vol. 108, 48, 19299-19304.

Cook, M.S., Keigwin, L.D., Birgel, D., Hirichs, K. (2011). Repeated pulses of vertical methane flux recorded in glacial sediments from the southeast Bering Sea.

Paleoceanography, 26, PA2210, doi;10.1029/2010PA001993.

Cook, M.S., Keigwin, L.D., Sancetta, C.A. (2005). The deglacial history of surface and intermediate water of the Bering Sea. Deep-Sea Research II, 52, 2163-2173.

Elderfield, H., Ferretti, P., Greaves, M., Crowhurst, S., McCave, I.N., Hodell, D., abd Piotrowski, A.M. (2012). Evolution of ocean temperature and Ice volume through the Mid-Pleistocene Climate Transition, Science, 10, vol. 337 no. 6095, pp. 704-709.

Fontanier, C., Jorissen, F.J., Michel, E., Cortijo, E., Vidal, L., Anshultz, P. (2008). Stable oxygen and carbon isotopes of live (stained) benthic foraminifera from Cap-Ferret Canyon (Bay of Biscay), Journal of Foraminiferal Research, 38, 39-51.

Fontanier, C., Mackensen, A., Jorissen F.J., Anschutz, P., Licari, L., Griveaud C. (2006). Stable oxygen and carbon isotopes of live benthic foraminifera from the Bay of Biscay: Microhabitat impact and seasonal cariability. Marine Micropaleontology, 58, 159-183.

Friedrich, O., Schiebel, R., Wilson, P.A., Weldeab, S., Beer, C.J., Cooper, M.J., Fiebig, J. (2012). Influence of test size, water depth, and ecology on Mg/Ca, Sr/Ca, $\delta^{18}O$, and $\delta^{13}C$ in nine modern species of planktic foraminifers, Earth and Planetary Science Letters, 319-320, 133-145.

Gebhardt, H., Sarnthein, M., Grootes, P.M., Kiefer, T., Kuehn, H., Schmieder, F., Röhl, U. (2008). Paleonutrient and productivity records from the subarctic North Pacific for Pleistocene glacial terminations I to V. Paleoceanography, 23, PA4212, doi:10.1029/2007PA001513.

Gorbarenko, S.A., Basov, I.A., Chekhovskaya, M.P., Southon, J., Khusid, T.A., Artemova,

A.V. (2005). Orbital and millennium scale environmental changes in the southern Bering Sea during the last glacial-Holocene: Geochemical and paleontological evidence. Deep-Sea Research II, 52, 2174-2185.

Gorbarenko, S.A., Khusid, T.A., Basov, I.A., Oba, T., Southon, J.R., Koizumi, I. (2002). Glacial Holocene environment of the southeastern Okhotsk Sea: evidence from geochemical and palaeontological data. Palaeogeography, Palaeoclimatology, Palaeoecology, 177, 237-263.

Gorbarenko, S.A., Southon, J.R., Keigwin, L.D., Cherepanova, M.V., Gvozdeva, I.G. (2004). Late Pleistocene-Holocene oceanographic variability in the Okhotsk Sea: geochemical, lithological and paleontological evidence. Palaeogeography, Palaeoclimatology, Palaeoecology, 209, 281-301.

Haug., G.H., Maslin, M.A., Sarnthein, M., Stax, R., Tiedermann, R. (1995). Evolution of northwest Pacific sedimentation patterns since 6 Ma (Site 882), Proceedings of Ocean Drilling Program: Scientific Results, 138, 371-412.

Hoogakker, B., Elderfield, H., Oliver, K., Crowhurst, S. (2010). Benthic foraminiferal oxygen isotope offsets over the last glacial-interglacial cycle, Paleoceanography, 25, PA4229, doi:10.1029/2009PA001870.

Hoshiba, M., Ahagon, N., Ohkushi, K., Uchida, M., Motoyama, I., Nishimura, A. (2006). Foraminiferal oxygen and carbon isotopes during the last 34 kyr off northern Japan, northwestern Pacific. Marine Micropaleontology, 61, 196-208.

Hovan, S.A., Rea, D.K., and Pisias, N.G. (1991). Late Pleistocene continental climate and oceanic variability recorded in northwest Pacific sediments, Paleoceanography, 6, 349-370.

Ishiwada, Y. (1964). Benthonic Foraminifera off the Pacific coast of Japan referred to

biostratigraphy of the Kazusa Group. Geological Survey of Japan Publishing, report No. 205, pp. 1-43.

Kanematsu, Y., Takahashi, K., Kim, S., Khim, B.K., Asahi, H. (2013). Changes in biogenic opal productivity with Milankovitch cycle during the last 1.3 Myrs at IODP Expedition 323 Sites U1341, U1343, and U1345 in the Bering Sea. Quaternary International, 310, 213-220.

Katsuki, K., Takahashi, K. (2005). Diatoms as paleoenvironmental proxies for seasonal productivity, sea-ice and surface circulation in the Bering Sea during the late Quaternary. Deep-Sea Research II, 52, 2110-2130.

Katsuki, K., Khim, B.K., Itaki, T., Harada, N., Sakai, H., Ikeda, T., Takaahshi, T., Okazaki, Y., Asahi, H. (2009). Land-sea linkage of Holocene paleoclimate on the Southern Bering Continental Shelf, The Holocene, 19, 747-756.

Keller, G. (1980). Benthic foraminifera and paleobathymetry of the Japan Trench area, Leg 57, deep sea drilling project. In: von Huene, R., Nasu, N. (Eds.) et al., Initial Reports of Ocean Drilling Program, 56-57 (1980), pp 835-865.

Kim, S., Khim, B.K., Uchida, M., Itaki, T., Tada, R. (2011). Millenial-scale paleoceanographic events and implication for the intermediate-water ventilation in the northern slope area of the Bering Sea during the last 71 kyrs. Global and Planetary Change, 79, 89-98.

Kim, S., Takahashi, K., Kanematsu, Y., Asahi, H., Ravelo, A.C., Khim, B.K. (in press) Mid-Pleistocene Transition in the Bering Sea: a continuous wavelet transform analysis of biogenic opal at IODP Expedition 323 Site U1343. Quaternary Research, available online 15 November, 2013, http://dx.doi.org/10.1016/j.yqres.2013.10.001

Kinney, J.C., Maslowski, W. (2012). On the oceanic communication between the Western Subarctic Gyre and the deep Bering Sea. Deep-Sea Research I, 66, 11-25.

Kukla, G., An, Z.S. (1989). Loess stratigraphy in central China, Palaeogeography, Palaeoclimatology, Palaeocology, 72, 203-225.

Lisiecki, L.E., Lisiecky, P.A. (2002). Application of dynamic programming to the correlation of paleoclimate records. Paleoceanography, 17, 1049, doi:10.1029/2001PA000733

Lisiecki, L.E., Raymo, M.E. (2005). A Pliocene–Pleistocene stack of 57 globally distributed benthic $\delta^{18}O$ records. Paleoceanography, 20, PA1003. doi:10.1029/2004PA001071

Lisiecki, L. E., Raymo, M.E. (2009). Diachronous benthic $\delta^{18}O$ responses during late Pleistocene terminations, Paleoceanography, 24, PA3210, doi:10.1029/2009PA001732.

Matoba, Y. (1967). Younger Cenozoic foraminiferal assemblages from the Choshi District, Chiba Prefecture. Science Reports of the Tohoku University, Sendai, Japan, Second Series (Geology), 38, No.2, 107-140.

McCorkle, D.C. Keigwin, K.D. (1990). The influence of microhabitats on the carbon isotopic composition of deep-sea benthic foraminifera, Paleoceanography, 5, 161-185.

McCorkle, D.C., Corliss, B.H., Farnham, C.A. (1997). Vertical distributions and stable isotopic composition of live (stained) benthic foraminifera from the North Carolina and California continental margins. Deep-Sea Research I, 44, 983-1024.

Mix, A.C., Le, J., Shackleton, N.J. (1995a). Benthic foraminiferal stable isotope stratigraphy of site 846: 0-1.8 Ma. Proceedings of the Ocean Drilling Program,

Scientific Results, 138, 839-854.

Mix, A.C., Pisias, N.G., Rugh, W., Wilson, J., Morey, A., Hagelberg, T.K. (1995b). Benthic foraminifer stable isotope record from Site 849 (0-5 Ma): local and global climate changes. Proceedings of the Ocean Drilling Program, Scientific Results, 138, 371-412.

Muhs, D.R., Ager, T.A., Bettis III, E.A., McGeehin, J., Been, J.M., Begét, J.E., Pacicch, M.J., Stafford, T.W. Jr., Stevens, D.S.P. (2003). Stratigraphy and paleoclimatic significance of late Quaternay loess-paleosol sequences of the last interglacial-glacial cycle in central Alaska, Quarternary Science Reviews, 22, 1947-1986.

Niebauer, H.J. (1998). Variability in Bering Sea ice cover as affected by a regime shift in the North Pacific in the period 1947-1996. Journal of Geophysical Research, 103, C12, 27717-27737.

Ohkushi, K., Ahagon, N., Uchida, M., Shibata, Y., (2005). Foraminiferal isotope anomalies from northwestern Pacific marginal sediments. Geochemistry, Geophysics, Geosystems, 6, 4, Q04005, doi:10.1029/2004GC000787.

Okazaki, Y., Takahashi, K., Asahi, H., Katsuki, K., Hori, J., Yasuda, H., Sagawa, Y., Tokuyama, H. (2005). Productivity changes in the Bering Sea during the late Quaternary. Deep-Sea Research II, 52, 2150-2162.

Okazaki, Y., Timmermann, A., Menviel, L., Harada, N., Abe-Ouchi, A., Chikamoto, M.O., Mouchet, A., Asahi, H. (2010). Deepwater formation in the North Pacific during the last glacial termination. Science, 329, 200-204.

Ono, A., Takahashi, K., Katsuki, K., Okazaki, Y., Sakamoto, T. (2005) The Dansgaard-Oeschger cycles discovered in the upstream source region of the

North Pacific Intermediate Water formation. Geophysical Research Letters, 32, L11607, doi:10.1029/2004GL022260.

Overland, J.E., Adams, J.M., Bond, N.A. (1999). Decadal variability of the Aleutian low and its relation to high-latitude circulation. Journal of Climate, 12, 1542-1548.

Paillard, D., Labeyrie L., Yiou, P. (1996). Macintosh program performs time-series analysis, Eos, Transactions American Geophysical Union, 77: 379.

Pease, C.H. (1980). Eastern Bering Sea ice processes. Monthly Weather Review, 108, 2015-2023.

Rella, S.F., Tada, R., Nagashima, K., Ikehara, M., Itaki, T., Ohkushi, K., Sakamoto, T., Harada, N., Uchida, M. (2012). Abrupt changes of intermediate water properties on the northeastern slope of the Bering Sea during the last glacial and deglacial period. Paleoceanography, 27, PA3203, doi:10.1029/2011PA002205.

Rodionov, S.N., Bond, N.A., Overland, J.E. (2007). The Aleutian Low, storm tracks, and winter climate variability in the Bering Sea. Deep-Sea Research II, 54, 2560-2577.

Rudnick, D.L., Davis, R.E. (2003). Red noise and regime shifts. Deep-Sea Research I, vol 50, 6, 691-699.

Sagawa, T., Ikehara, K. (2008). Intermediate water ventilation change in the subarctic northwest Pacific during the last deglaciation, Geophyisical Research Letters, 35, L24702, doi:10.1029/2008GL035133.

Saidova, Kh, M. (1961). Foraminiferal ecology and paleogeography, Far Eastern seas of the USSR and northwest part of the Pacific Ocean. Nauka, Moscow, pp. 1-232.

Sakamoto, T., Ikehara, M., Aoki, K., Iijima, K., Kimura, N., Nakatsuka, T., Wakatsuchi, M. (2005). Ice-rafted debris (IRD)-based sea-ice expansion events during the past

100 kyrs in the Okhotsk Sea. Deep-Sea Research II, 52, 2275-2301.

Schlung, S.A., Ravelo, A.C., Aiello, I.W., Andreasen, D.H., Cook, M.S., Drake, M., Dyez, K.A., Gullderson, T.P., LaRiviere, J., Stroynowski, Z., Takahashi. K. (2013). Millennial-scale climate change and intermediate water circulation in the Bering Sea from 90 ka ; A high-resolution record from IODP Site U1340. Paleoceanography, doi:10.1029/2012PA002365.

Schmiedl, G., Pfeilsticker, M., Hemleben, C., and Mackensen, A. (2004). Environmental and biological effects on the stable isotope composition of Recent deep-sea benthic foraminifera from the Mediterranean Sea, Marine Micropaleontology, 51, 1-2, 129-152.

Schönfeld, J. (2006). Taxonomy and distribution of the *Uvigerina peregrina* plexus in the tropical to Northeastern Atlantic. Journal of Foraminiferal Research, 36, 355-367.

Shackleton, N.J. (1974). Attainment of isotopic equilibrium between ocean water and the benthonic foraminifera genus *Uvigerina*: isotopic changes in the ocean during the last glacial. Les Méthodes Quantitatives Détude, Des Variations du Climat au Cours du Pléistocéne, Colloques Internationaux du C.N.R.S., 219:203-209

Shackleton, N.J., Hall, M.A., Pate, D. (1995). Pliocene stable isotope stratigraphy of Site 846. Proceedings of the Ocean Drilling Program, Scientific Results, 138, 337-355.

Skinner, L.C., Shackleton, N.J. (2005). An Atlantic lead over Pacific deep-water change across Termination I : Implications for the application of the marine isotope stage stratigraphy, Quaternary Science Reviews, 24, 571-580.

Spero, H.J., Lea, D.W. (1996). Experimental determination of stable isotope variability in *Globigerina bulloides*: implications for paleoceanographic reconstructions.

Marine Micropaleontology, 28, 231-246.

Stabeno, P.J., Schumacher, J.D., Ohtani, K. (1999). The physical oceanography of the Bering Sea, in Loughlin, T.R., and Ohtani, K., eds., Dynamics of the Bering Sea: A summary of Physical. Chemical, and Biological Characteristics, and a Synopsis of the Bering Sea, North Pacific marine Science Organization (PICES), University of Alaska Sea Grant, AK-SG-99-03, p. 1-28.

Sun, Y. and An, Z. (2005). Late Pliocene-Pleistocene changes in mass accumulation rates of eolian deposits on the central Chinese Loess Plateau. Journal of Geophysical Research, 110, D23101. doi:10.1029/2005JD006064.

Takahashi, K. (2005). The Bering Sea and paleoceanography. Deep-Sea Research II, 52, 16-18.

Takahashi, K., Ravelo, A. C., Alvarez-Zarikian. C. A., the Expedition 323 Scientists (2011). Bering Sea Paleoceanography**.** Proc. IODP Exp. Rept*.,* 323、Tokyo (Integrated Ocean Drilling Program Management International, Inc.). doi:10.2204/iodp.proc.323.2011.

Tanaka, S., Takahashi, K. (2005). Late Quaternary paleoceanographic changes in the Bering Sea and the western subarctic Pacific based on radiolarian assemblages. Deep-Sea Research II, 52, 2131-2149.

Teraishi, A., Suto, I., Onodera, J., Takahashi, K. (in press). Diatom, silicoflagellate and ebridian biostratigraphy and paleoceanography in IODP 323 Hole U1343E at the Bering Slope site. Deep-Sea Research II , available online 13 March, 2013, http://dx.doi.org/10.1016/j.dsr2.2013.03.026i

Torrence, C., Compo, G.P. (1998). A Practical Guide to Wavelet Analysis. Bulletin of the

American Meteorological Society, 79, 1, 61-78.

Tziperman, E., Gildor, H. (2003). On the mid-Pleistocene transition to 100-kyr glacial cycles and the asymmetry between glaciation and deglaciation times. Paleoceanography, 18, 1001. doi: 10.1029/2001PA000627

Venti, N.L., Billups, K. (2012). Stable-isotope stratigraphy of the northwest Pacific during the Pliocene-Pleistocene climate transition, Palaeogeography, Palaeoclimatology, and Palaeoecology, 326-328:54-65.

Venti, N.L., Billups, K., and Herbert, T.D. (2013). Inceased sensitivity of the Plio-Pleistocene northwest Pacific to obliquity forcing. Earth and Planetary Science Letters, 384, 121-131.

Vergnaud Grazzini, C. (1976). Non-equilibrium isotopic compositions of shells of planktonic foraminifera in the Mediterranean Sea. Palaeogeography, Palaeoclimatology, Palaeoecology, 20, 263-276.

Zahn, R., Mix, A.C. (1991). Benthic foraminiferal $\delta^{18}O$ in the ocean's temperature-salinity-density field: constraints on ice age thermohaline circulation. Paleoceanography, 6, 1-20

Zhang, J.Z., Woodgate, R., Moritz, R. (2010). Sea ice response to atmospheric and oceanic forcing in the Bering Sea. Journal of Physical Oceanography, 40, 1729-1747.

Figure captions

Figure 1. Map showing (a) the location of IODP Expedition 323 Site U1343 and other drilled sites, the modern sea-ice edge in February (Cavalieri et al., 1996), and surface water circulation, and (b) cross section of the passages along the Aleutian Islands. Numbers in parenthesis are the model-calculated volume flux of northward (positive) and southward (negative) flow at each passage (Kinney and Maslowski, 2012). BSC: the Bering Slope Current, AS: the Alaskan Stream, SC: the subarctic current. Note that corresponding numbers (1) to (7) in both map and cross section indicate the location of major passages between the Bering Sea and the North Pacific.

Figure 2. Correlation of the species-specific $\delta^{18}O$ offset between the six species of benthic foraminfera and *Elphidium batialis* at Site U1343.

Figure 3. Plots of seven benthic foraminiferal $\delta^{18}O$ records at Site U1343 against sediment depth. Note that panel (a) shows actual measured $\delta^{18}O$ values, whilst panel (b) shows $\delta^{18}O$ records after a species-specific correction was applied (derived from Fig. 2).

Figure 4. Depth-age plot showing the orbital-scale oxygen isotope stratigraphy (black line) with biostratigraphic and paleomagnetic datums (diatom: Teraishi et al., in press; other datums: Takahashi et al., 2011).

Figure 5. Comparison of the 2.4 Myrs records of (a) global stack curve "LR04" (Lisiecki and Raymo, 2005) and composite oxygen isotope records of benthic foraminifera, and 1.5-kyr running means of (b) magnetic susceptibility (MS) (c) natural gamma-ray radiation (NGR), (d) gamma ray attenuation (GRA), (e) linear sedimentation rate (LSR) at Site U1343. Note that all physical property data were taken from Takahashi et al. (2011).

Figure 6. Blackman-Tukey spectra of (a) $\delta^{18}O$, (b) GRA, (c) NGR, and (d) MS in different time windows (all time intervals, 0-0.8 Ma, 0.8-1.2 Ma, and 1.2-2.4 Ma) at Site U1343. Note that error bars are estimated with 80% confidence level.

Figure 7. Continuous wavelet transform of (a) LR04, (b) $\delta^{18}O$, and (c) their coherency (contours) and phase angle (arrows) at Site U1343. Note that thick black line contours represent 90% confidence level by assuming the red noise as background spectrum.

Figure 8. Band-pass filtered variability of LR04 and $\delta^{18}O$, GRA, NGR, and MS at Site U1343, in different time domains (a) 100-kyr and (b) 41 kyr.

Figure 9. Continuous wavelet transform of (a) GRA, (b) NGR, and (c) MS at Site U1343. Note that black line contours represent 90% confidence level by assuming the red noise (thick black line) and the white noise (dashed black line) as their background spectrum.

Figure 10. Cross wavelet coherencies (contours) and phase angles (arrows) of (a) GRA, (b) NGR, and (c) MS to $\delta^{18}O$ at Site U1343. Note that upward direction of arrows indicate subjected data are in phase, whereas downward direction indicates out of phase.

Figure 11. Coherencies (dotted line) and time differences (bar) between $\delta^{18}O$ and the physical properties (GRA, NGR and MS) at eccentricity (100-kyr) and obliquity (41-kyr) domain in the arbitrary time at Site U1343. Dash lines in coherency columns represent 80, 90, 95, 99% confident level, respectively. Note that time differences are only calculated when coherencies exceeded 80% confidence level.

Figure 12. Detailed comparison of the oxygen isotope stratigraphy (a and d) with the physical properties (MS: b and f; NGR: c and g; and GRA: d and h) during 0-1.2 Ma (a-d) and 1.2-2.4 Ma (e-h).

Table 1. Species-specific offsets of $\delta^{18}O$ values to *E. batialis* at Site U1343, their $\Delta\delta^{18}O_{water\text{-}calcite}$, and their previously published $\Delta\delta^{18}O_{water\text{-}calcite}$ (Basak et al., 2009; Fontanier et al, 2008; McCorkle et al., 1997). Note that $\Delta\delta^{18}O_{water\text{-}calcite}$ at Site U1343 was estimated on the basis of the modern $\Delta\delta^{18}O_{water\text{-}calcite}$ of *G. pacifica* in the Aleutian Basin (Basak et al., 2009).

Appendix 1. Depth-age time of tie points at the Marine Isotope Stage (MIS) boundary at

Site U1343 derived from the oxygen isotope stratigraphy in this study.

Appendix 2. All depth-age time of tie points at Site U1343 derived from the oxygen isotope stratigraphy in this study.

MIS Boundary	Age (Ma)	Depth (m CCSF-A)
core top	0.00762	0.010
1/2	0.014	3.191
2/3	0.029	7.523
3/4	0.057	13.158
4/5	0.071	18.415
5/6	0.13	38.550
6/7	0.191	48.766
7/8	0.243	71.613
8/9	0.3	87.122
9/10	0.337	95.582
10/11	0.374	107.628
11/12	0.424	119.603
12/13	0.478	128.193
13/14	0.533	149.518
14/15	0.563	155.331
15/16	0.621	170.886
16/17	0.676	177.286
17/18	0.712	184.047
18/19	0.761	195.749
19/20	0.79	203.287
20/21	0.814	213.459
21/22	0.866	225.850
22/23	0.9	232.177
23/24	0.917	237.544
24/25	0.936	245.205
25/26	0.959	253.764

26/27	0.97	260.243
27/28	0.982	265.362
28/29	1.014	276.371
29/30	1.031	284.267
30/31	1.062	294.770
31/32	1.081	304.129
32/33	1.104	311.234
33/34	1.114	317.405
34/35	1.141	326.016
35/36	1.19	338.115
36/37	1.215	349.186
37/38	1.244	360.714
38/39	1.264	372.202
39/40	1.286	382.438
40/41	1.304	390.786
41/42	1.32	398.140
42/43	1.344	405.807
43/44	1.362	411.486
44/45	1.383	416.457
45/46	1.405	421.550
46/47	1.424	426.886
47/48	1.452	432.700
48/49	1.469	440.073
49/50	1.492	445.915
50/51	1.51	450.705
51/52	1.53	455.406
52/53	1.5475	462.090
53/54	1.57	468.260
54/55	1.585	472.952
55/56	1.608	477.893
56/57	1.6285	482.622
57/58	1.6425	487.485
58/59	1.67	495.941
59/60	1.6975	505.496
60/61	1.715	515.239
61/62	1.743	526.051
62/63	1.758	534.106
63/64	1.782	539.490
64/65	1.8025	543.962

65/66	1.816	547.230
66/67	1.826	549.503
67/68	1.8325	551.748
68/69	1.849	554.590
69/70	1.8595	557.603
70/71	1.875	561.304
71/72	1.898	566.708
72/73	1.915	574.519
73/74	1.941	583.872
74/75	1.965	593.875
75/76	1.99	604.081
76/77	2.017	614.691
77/78	2.043	627.148
78/79	2.088	637.475
79/80	2.103	645.179
80/81	2.125	654.167
81/82	2.146	664.936
82/83	2.168	674.742
83/84	2.192	683.415
84/85	2.2075	692.969
85/86	2.236	703.866
86/87	2.25	713.943
87/88	2.273	726.828
88/89	2.291	739.125
89/90	2.309	748.983
90/91	2.333	759.466
91/92	2.35	769.697
92/93	2.373	779.423
93/94	2.387	N/A

Age (Ma)	Depth (m CCSF-A)
0.00762	0.010
0.01778	3.860
0.02032	4.630
0.03302	7.710
0.04572	10.789
0.04826	11.559
0.05080	12.329
0.05334	13.099
0.05588	13.869
0.05842	14.639
0.06096	15.409
0.06350	16.179
0.06604	16.949
0.06858	17.719
0.07874	21.569
0.08890	25.419
0.09906	29.269
0.10922	33.118
0.11176	33.888
0.11938	35.428
0.13208	36.968
0.14478	38.508
0.14986	39.278
0.15748	40.818
0.16764	43.128

0.17018	43.898
0.18034	47.748
0.19050	51.597
0.20066	55.447
0.20320	56.217
0.21590	59.297
0.21844	60.067
0.22860	63.917
0.23876	67.767
0.24892	71.616
0.25146	72.386
0.25400	73.156
0.25654	73.926
0.25908	74.696
0.27178	77.776
0.27432	78.546
0.27686	79.316
0.27940	80.086
0.28194	80.856
0.28448	81.626
0.29718	84.706
0.30988	87.785
0.31242	88.555
0.31496	89.325
0.31750	90.095
0.32004	90.865
0.32258	91.635
0.32512	92.405
0.32766	93.175
0.33020	93.945
0.33274	94.715
0.34544	97.795
0.35814	100.875
0.36068	101.645
0.36322	102.415
0.36576	103.185
0.37592	107.034
0.38608	110.884
0.39624	114.734

0.39878	115.504
0.40640	117.044
0.41148	117.814
0.42418	119.354
0.42926	120.124
0.43434	120.894
0.43942	121.664
0.44450	122.434
0.45720	124.744
0.46482	126.283
0.47498	128.593
0.47752	129.363
0.48006	130.133
0.49022	133.983
0.49784	137.063
0.50546	140.143
0.51562	143.993
0.51816	144.762
0.52070	145.532
0.52324	146.302
0.53594	149.382
0.54864	152.462
0.56134	155.542
0.56388	156.312
0.56642	157.082
0.57658	160.932
0.57912	161.702
0.58928	164.011
0.59690	165.551
0.60452	167.091
0.61214	168.631
0.62484	170.941
0.63754	172.481
0.65024	174.021
0.66294	175.561
0.67564	177.871
0.68326	179.411
0.69088	180.951
0.69850	182.490

0.70612	184.030
0.71374	185.570
0.72644	187.880
0.73914	190.190
0.74676	191.730
0.75692	194.040
0.76962	197.120
0.77216	197.890
0.77470	198.660
0.77724	199.430
0.77978	200.200
0.78232	200.970
0.79248	204.819
0.79502	205.589
0.80772	208.669
0.81026	209.439
0.81280	210.209
0.82296	214.059
0.83312	217.909
0.84328	221.758
0.84582	222.528
0.85852	225.608
0.86614	227.148
0.87122	227.918
0.87630	228.688
0.88138	229.458
0.89408	231.768
0.90170	233.308
0.91186	235.618
0.91440	236.388
0.91694	237.158
0.92710	241.007
0.93472	244.087
0.93980	246.397
0.94488	248.707
0.94996	251.017
0.95504	253.327
0.96012	255.637
0.96520	257.947

0.97028	260.256
0.97536	262.566
0.98044	264.876
0.98806	267.956
0.99822	271.806
1.00076	272.576
1.00330	273.346
1.00584	274.116
1.00838	274.886
1.01092	275.656
1.01346	276.426
1.01600	277.196
1.02616	281.045
1.03632	284.895
1.04394	287.975
1.04902	290.285
1.05410	292.595
1.05918	294.905
1.06426	297.215
1.07188	300.294
1.08204	304.144
1.09220	307.994
1.10236	311.844
1.11252	315.694
1.11506	316.464
1.11760	317.233
1.12014	318.003
1.12268	318.773
1.12522	319.543
1.12776	320.313
1.13030	321.083
1.13284	321.853
1.13538	322.623
1.13792	323.393
1.14046	324.163
1.14300	324.933
1.14554	325.703
1.14808	326.473
1.15062	327.243

1.15316	328.013
1.15570	328.783
1.15824	329.553
1.16078	330.323
1.17094	334.173
1.17348	334.943
1.17602	335.713
1.17856	336.482
1.18110	337.252
1.18364	338.022
1.18618	338.792
1.18872	339.562
1.19126	340.332
1.19380	341.102
1.19634	341.872
1.19888	342.642
1.20904	346.492
1.21920	350.342
1.22682	353.422
1.23190	355.732
1.23952	359.581
1.24714	363.431
1.25476	367.281
1.26238	371.131
1.27000	374.980
1.27762	378.830
1.28524	382.680
1.29032	384.990
1.29540	387.300
1.30048	389.610
1.30810	392.690
1.31572	395.769
1.32588	399.619
1.33604	403.469
1.34620	407.319
1.34874	408.089
1.36144	411.169
1.37414	414.248
1.38684	417.328

1.39954	420.408
1.41224	423.488
1.42494	426.568
1.43764	429.648
1.45034	432.727
1.45288	433.497
1.46304	437.347
1.47320	441.197
1.47574	441.967
1.47828	442.737
1.48082	443.507
1.49352	446.587
1.50622	449.667
1.51892	452.746
1.53162	455.826
1.53416	456.596
1.54432	460.446
1.55448	464.296
1.55702	465.066
1.55956	465.836
1.56210	466.606
1.56464	467.376
1.56718	468.146
1.57988	471.225
1.59258	474.305
1.60528	477.385
1.61798	480.465
1.63068	483.545
1.64338	486.625
1.64592	487.395
1.64846	488.165
1.65100	488.935
1.65354	489.705
1.66370	493.554
1.67386	497.404
1.68402	501.254
1.69418	505.104
1.70180	508.184
1.70942	511.263

1.71450	513.573
1.72212	517.423
1.72974	521.273
1.73736	525.123
1.74244	527.433
1.75006	530.512
1.76022	534.362
1.76276	535.132
1.77546	538.212
1.78562	540.522
1.79578	542.832
1.80594	545.142
1.81610	547.452
1.82626	549.761
1.83642	552.071
1.84658	554.381
1.85674	556.691
1.86690	559.001
1.87706	561.311
1.88976	564.391
1.89230	565.161
1.89484	565.931
1.90500	569.780
1.91516	573.630
1.92278	576.710
1.93040	579.790
1.93802	582.870
1.94564	585.950
1.95326	589.029
1.96088	592.109
1.96850	595.189
1.97612	598.269
1.98374	601.349
1.99136	604.429
1.99898	607.508
2.00660	610.588
2.01422	613.668
2.02184	616.748
2.02946	619.828

2.03708	622.908
2.04470	625.987
2.05232	629.067
2.06248	632.917
2.06502	633.687
2.07772	636.767
2.09042	639.847
2.09296	640.617
2.10312	644.466
2.11074	647.546
2.11582	649.856
2.12090	652.166
2.12852	656.016
2.13614	659.866
2.14376	663.715
2.15138	667.565
2.15646	669.875
2.16408	672.955
2.17170	676.035
2.17932	679.115
2.18694	682.195
2.19456	685.274
2.19964	687.584
2.20472	689.894
2.21234	693.744
2.21996	697.594
2.22758	701.443
2.23520	705.293
2.24282	709.143
2.25044	712.993
2.25806	716.843
2.26060	718.383
2.26568	722.232
2.27076	726.082
2.27584	729.932
2.28092	733.782
2.28346	735.322
2.29108	739.172
2.29870	743.021

2.30632	746.871
2.31394	750.721
2.32156	754.571
2.32918	758.421
2.33680	762.270
2.34442	766.120
2.35204	769.970

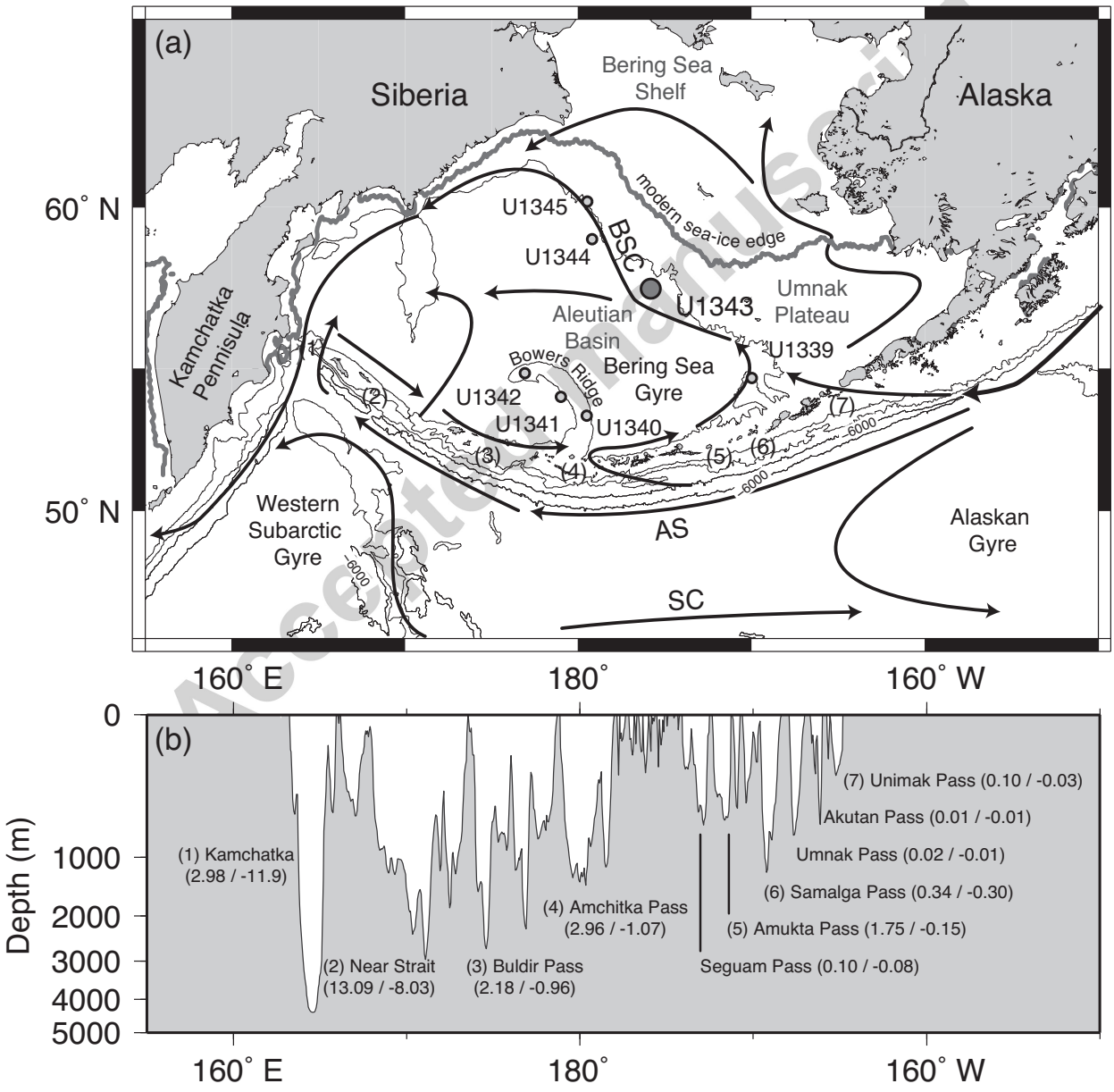

Fig. 1 Asahi et al

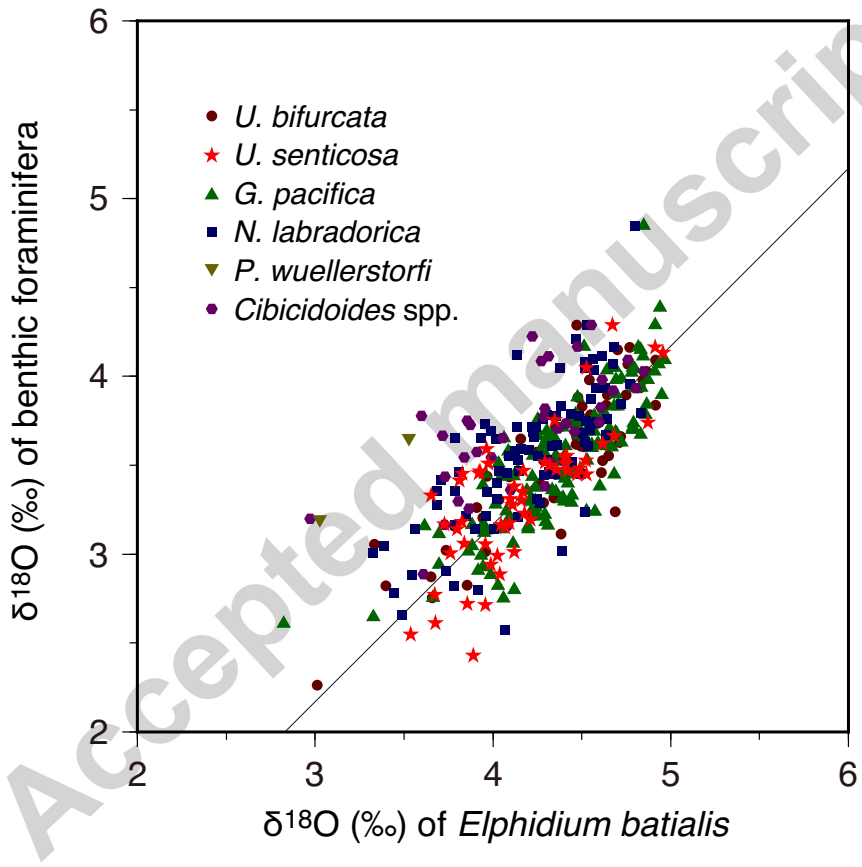

Fig. 2. Asahi et al

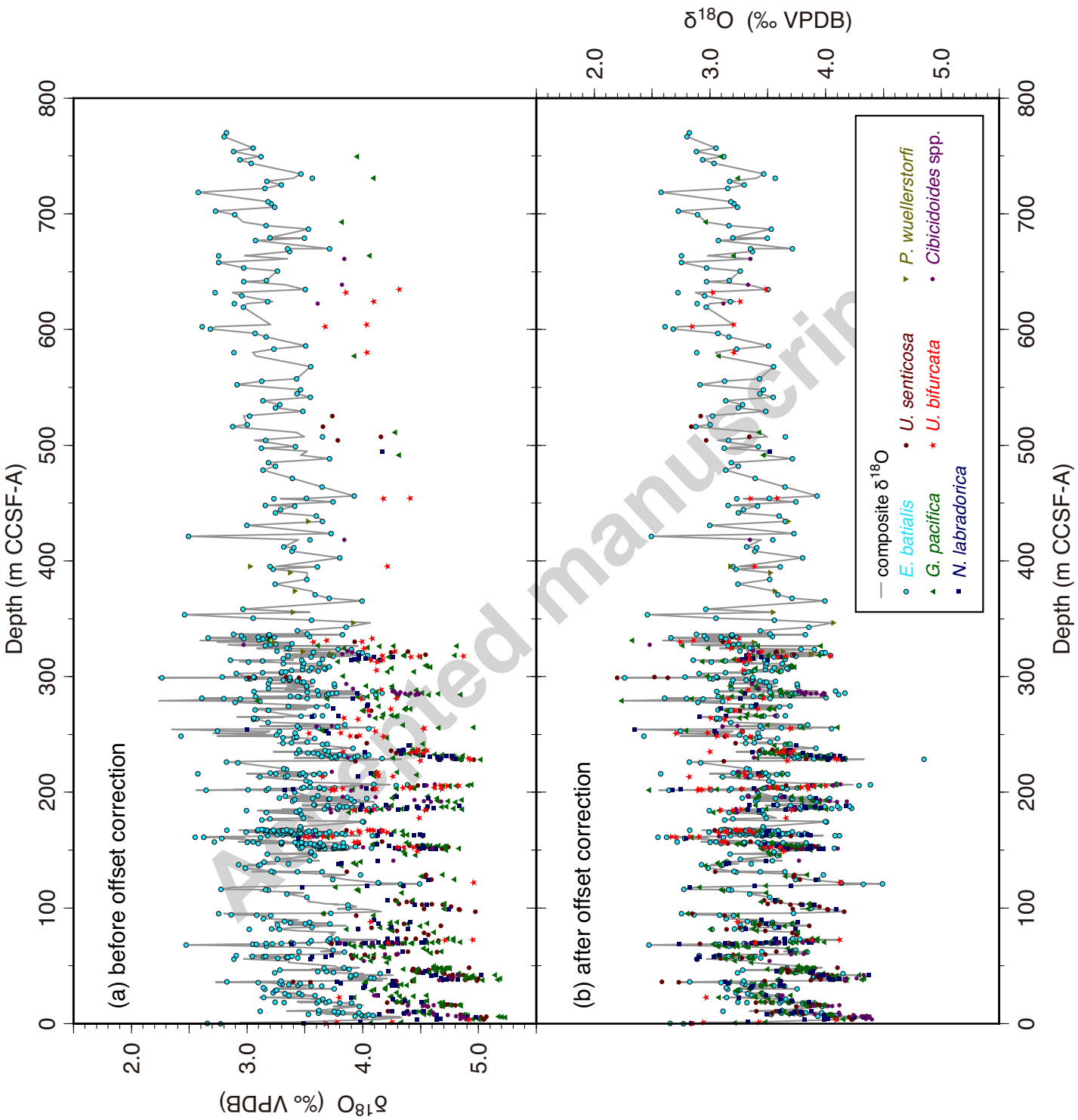

Fig. 3. Asahi et al.

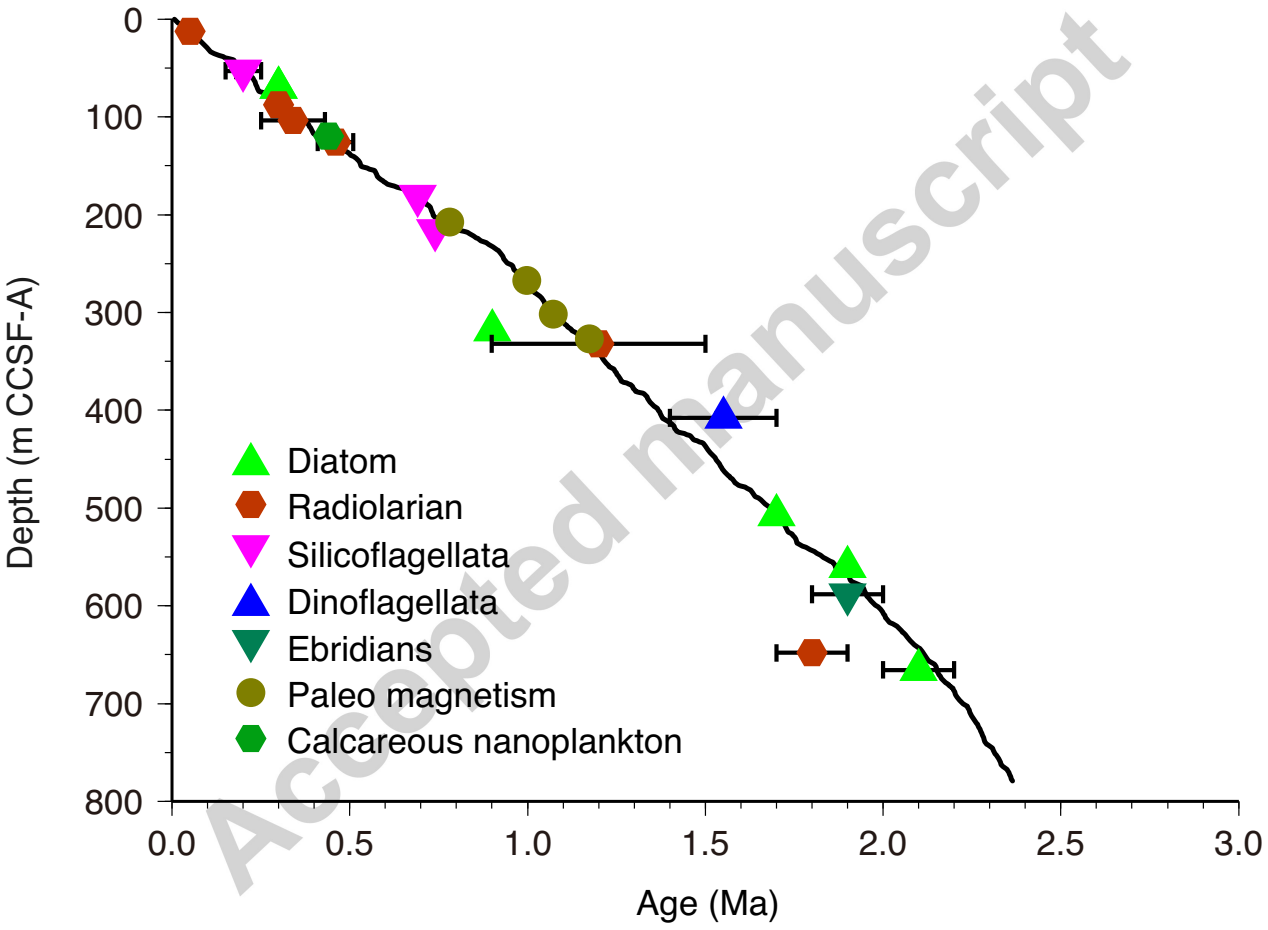

Fig. 4. Asahi et al.

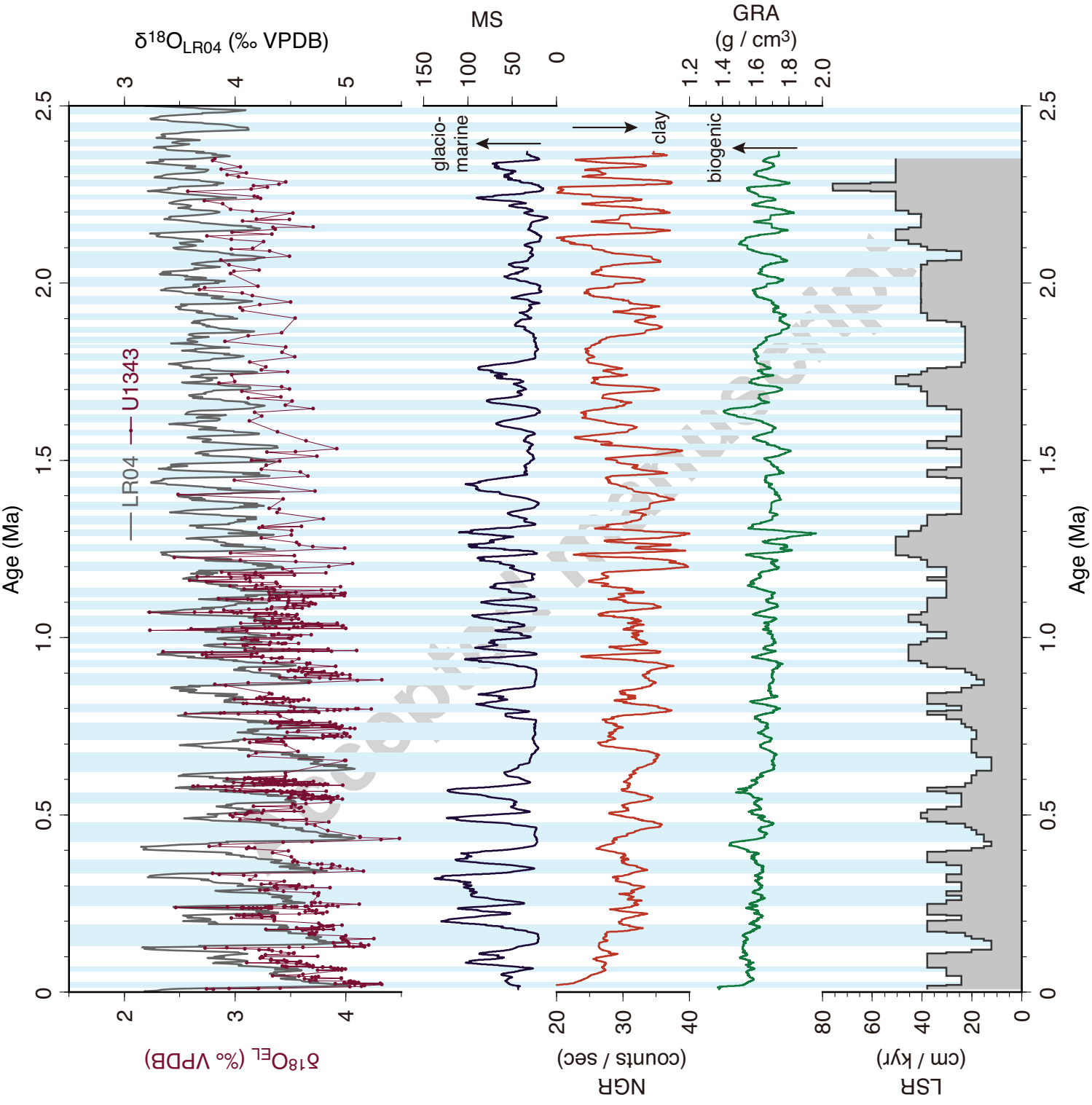

Fig. 5. Asahi et al.

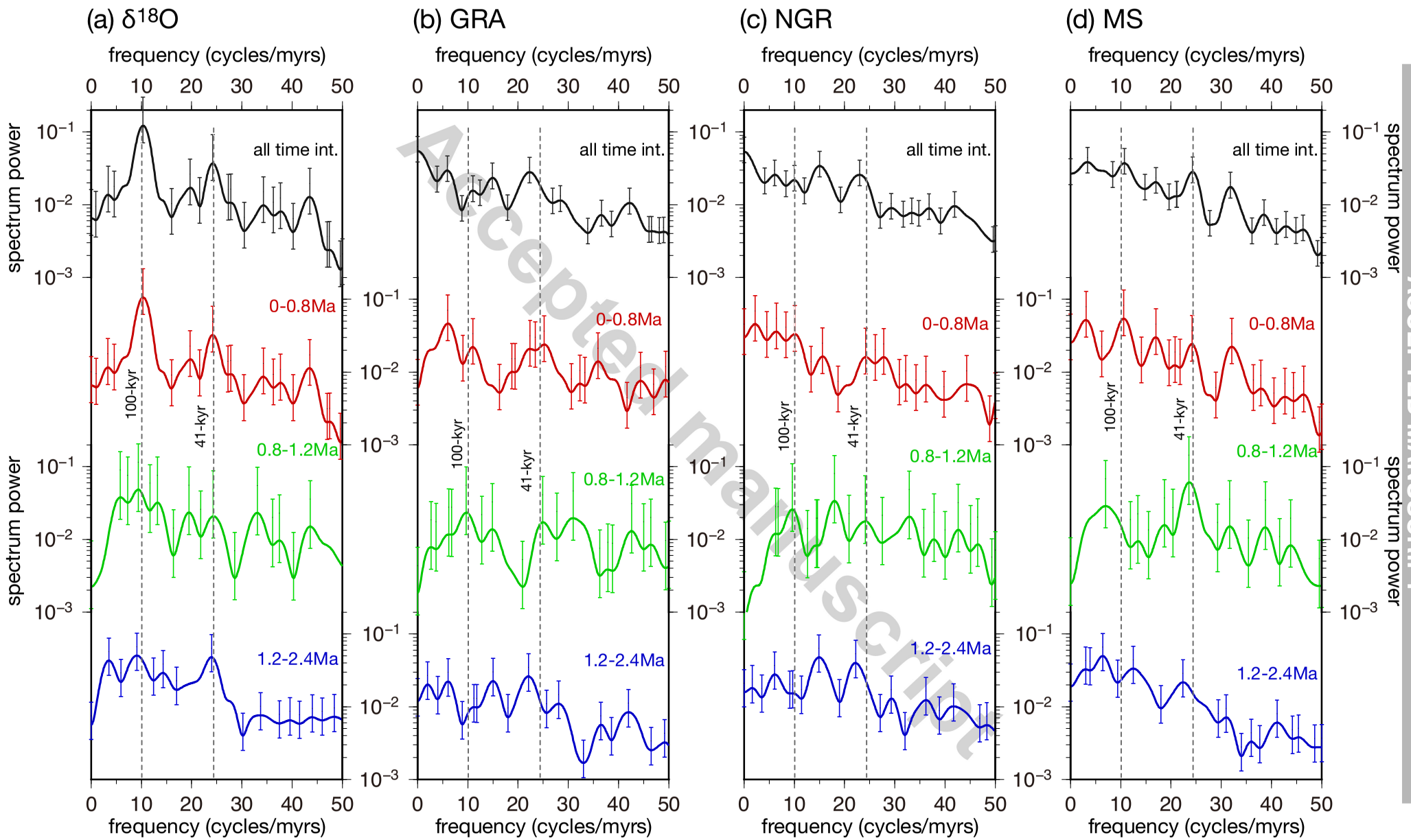

Fig. 6. Asahi et al.

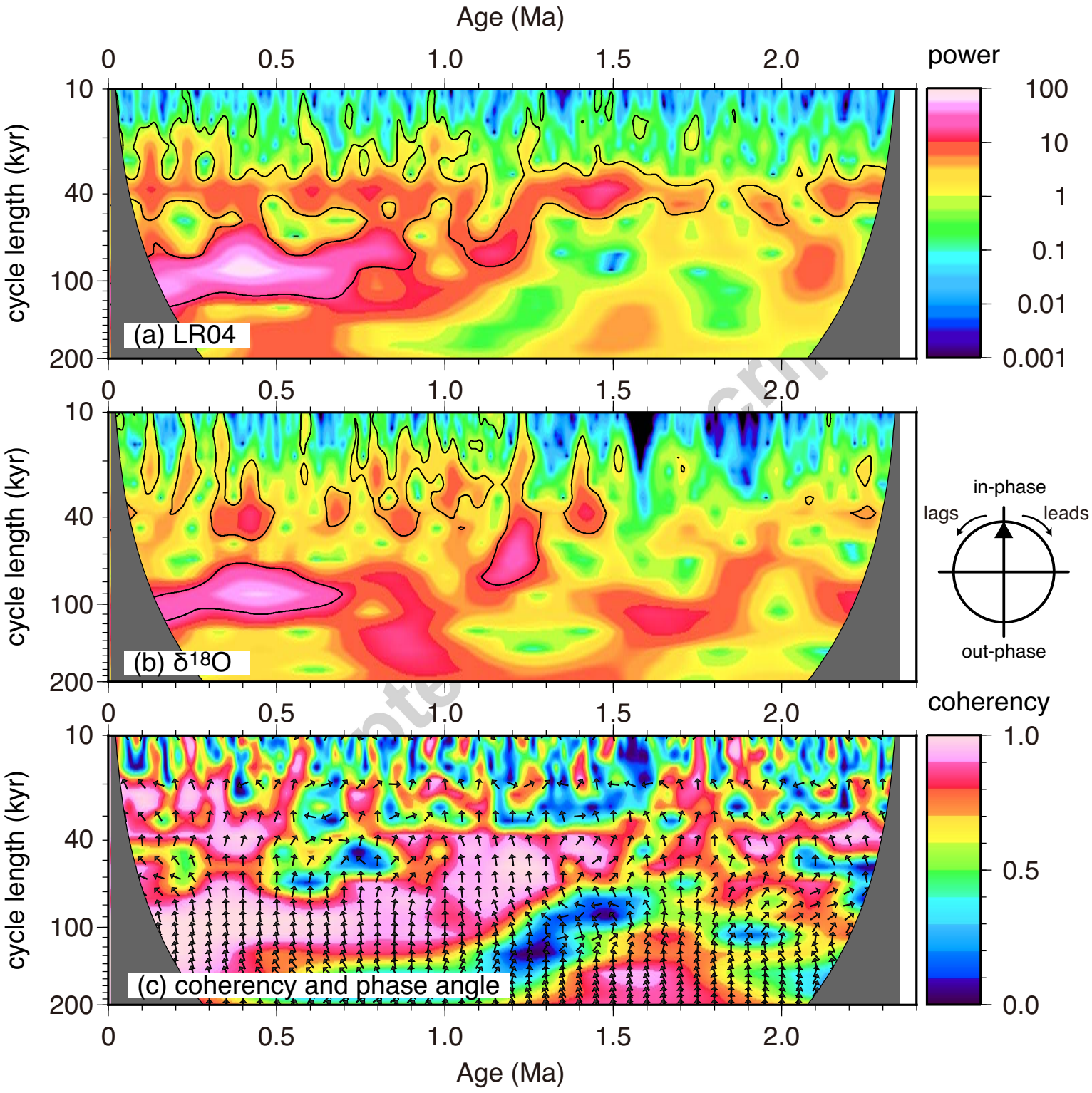

Fig. 7. Asahi et al.

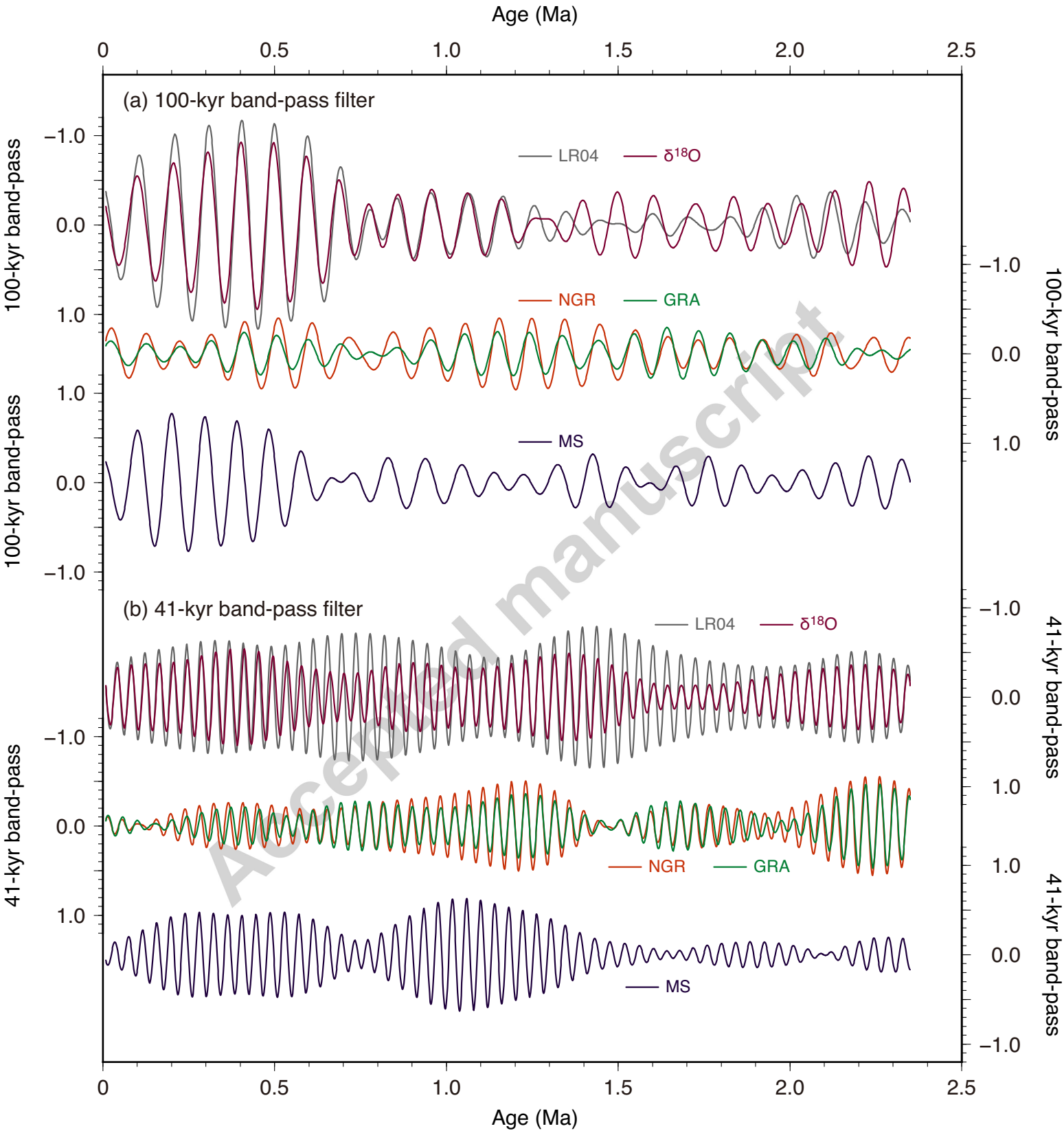

Fig. 8. Asahi et al

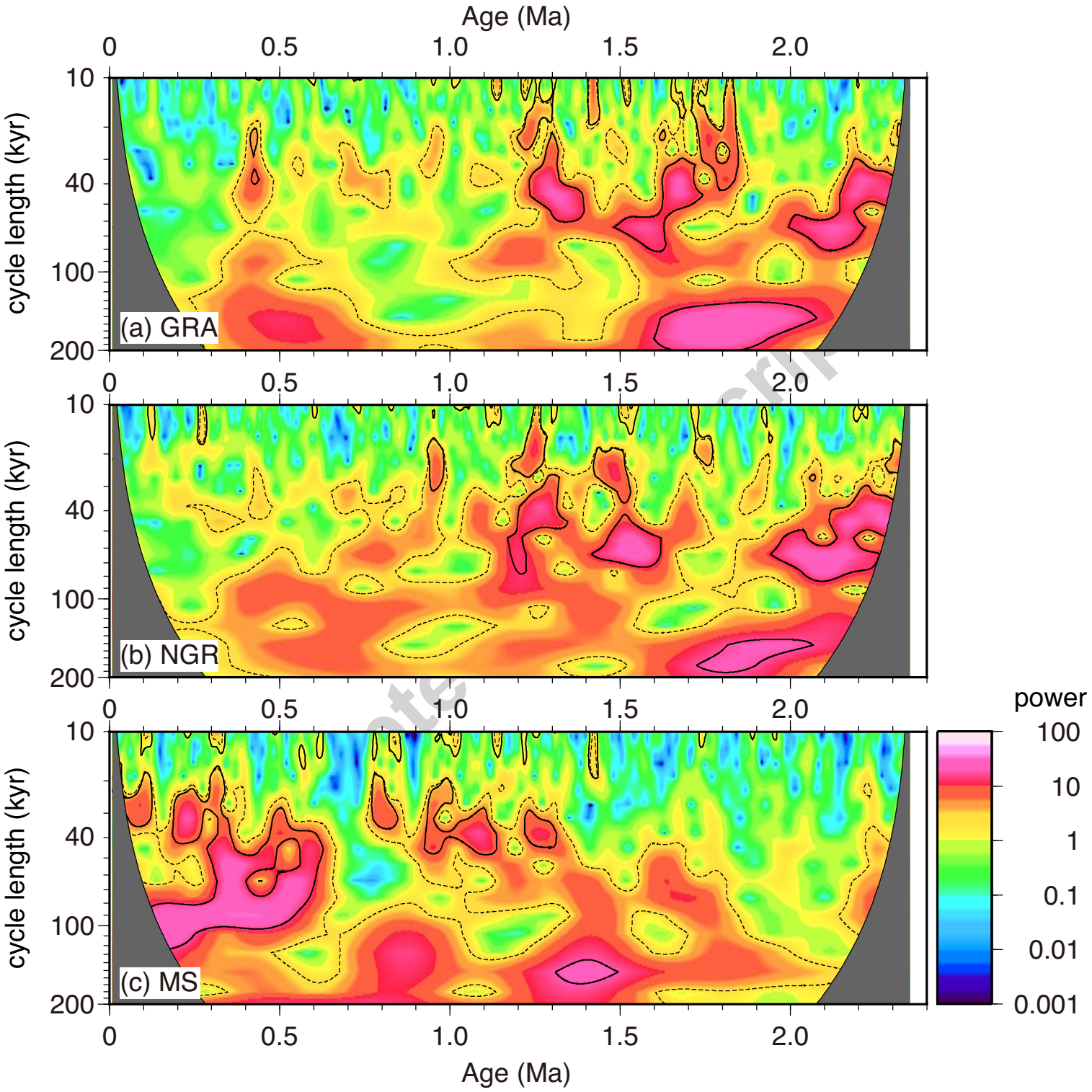

Fig. 9. Asahi et al.

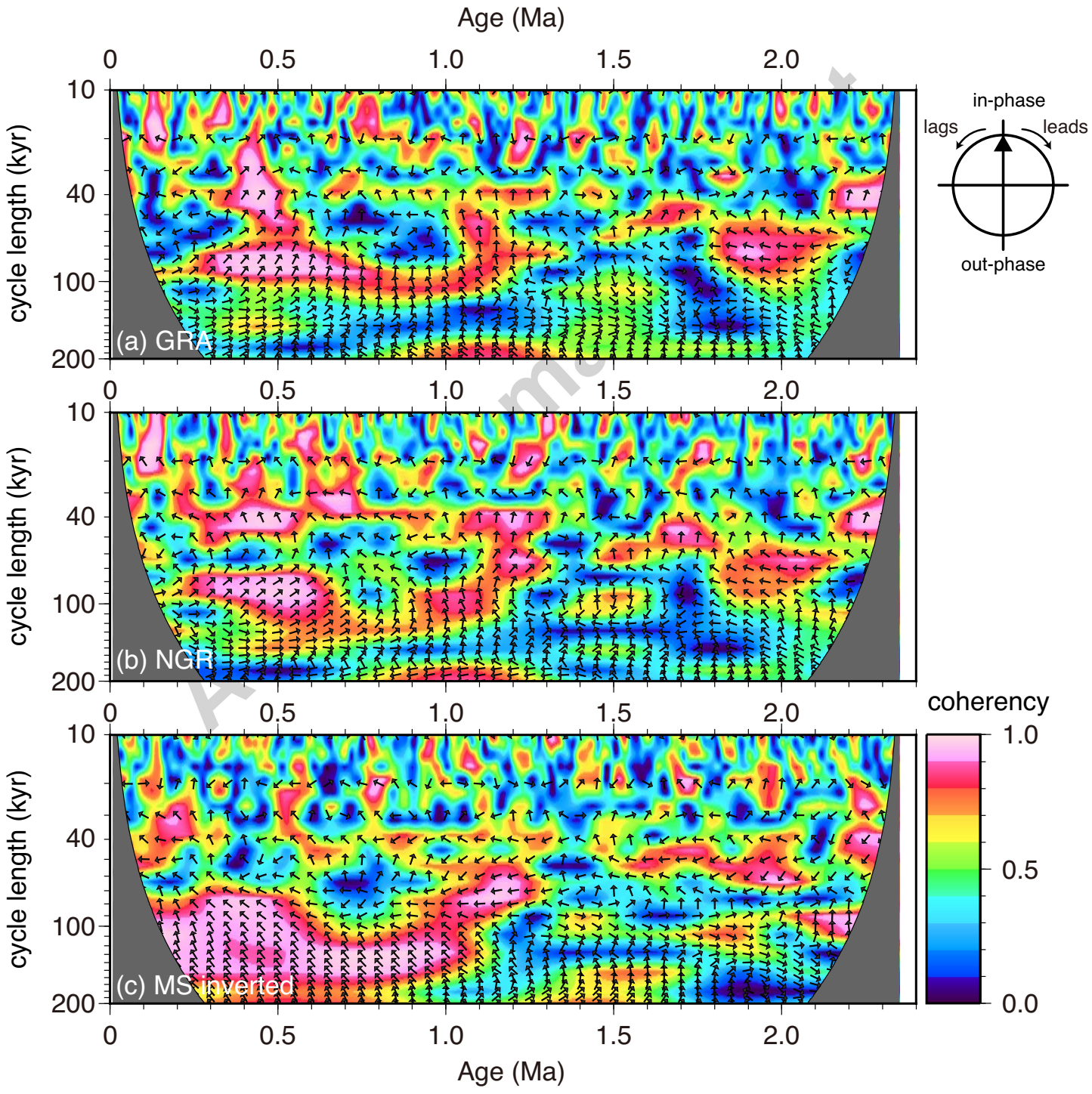

Fig. 10. Asahi et al.

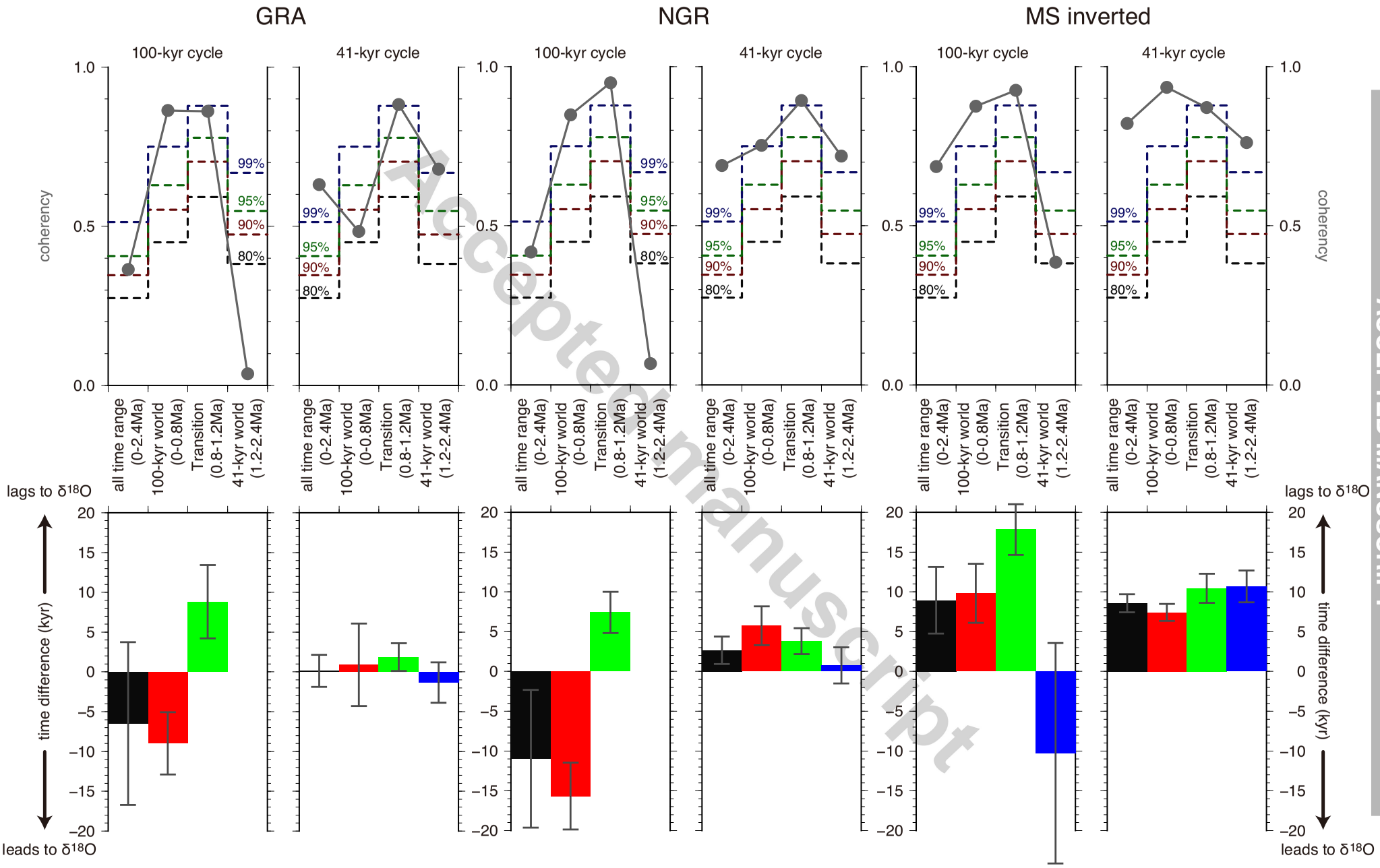

Figure 11. Asahi et al. (revised)

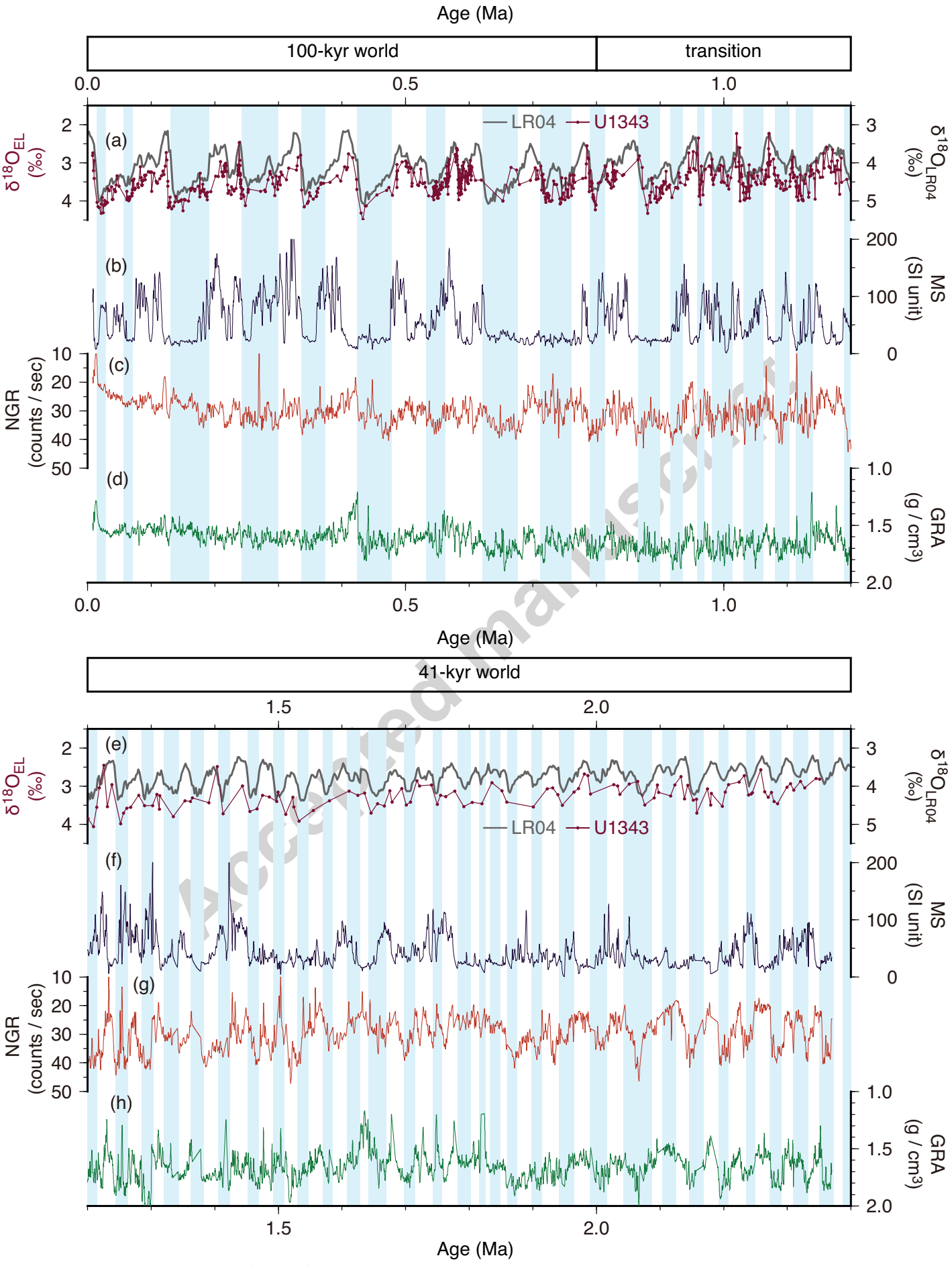

Fig. 12. Asahi et al.

	This study			Published data							
	offsets to *E. batialis* (‰ VPDB)			offsets to bottom water (‰ VPDB)						sp. name	reference
	ofsets*	(stdev)	n	$\Delta\delta^{18}O_{water\text{-}calcite}$**	$\Delta\delta^{18}O_{water\text{-}calcite}$	(stdev)	Region	$\Delta\delta^{18}O_{water\text{-}calcite}$	(stdev)	Region	
Cibicidoides spp.	0.49	(0.32)	36	-0.15	-0.91	(0.11)	Pacific	-0.67	(0.36)	Atlantic	all *Cibicidoides*	McCorkle et al. (1997)
G. pacifica	0.86	(0.21)	147	0.21	-0.01	(0.11)	Pacific	0.17	(0.32)	Atlantic	*G. affinis/pacifica*	McCorkle et al. (1997)
					0.21		Aleutian Basin				*G. pacifica*	Basak et al. (2009)
								-0.04		N. Atlantic	*Globobulimina* spp.	Fontanier et al. (2006)
E. batialis	0	(N/A)	N/A	-0.65	N/A			N/A			N/A	N/A
N. labradorica	0.65	(0.27)	91	0.00				-0.01	(0.20)	Atlantic	*F. labradorica*	McCorkle et al. (1997)
U. bifurcata	0.83	(0.25)	53	0.18	-0.09	(0.07)	Pacific	-0.12	(0.09)	Atlantic	*U. peregrina*	McCorkle et al. (1997)
								-0.37		N. Atlantic	*U. peregrina*	Fontanier et al. (2006)
U. senticosa	0.82	(0.22)	61	0.17	N/A			N/A			N/A	N/A
P. wuellerstorfi	-0.15	(0.03)	2	-0.80	-0.90	(0.11)	Pacific				*C. wuelfstori*	McCorkle et al. (1997)

*: calculated based on the specie-sepcific offset to *E. batiaris*

**: calculated based on the modern Δ δ18Owater-calcite of *G. pacifica* at the Aleutian Basin (Basak et al., 2009)

Table 1 Asahi et al